



Published in final edited form as:

J Mol Cell Cardiol. 2016 October ; 99: 174–187. doi:10.1016/j.yjmcc.2016.06.068.

Modeling Na⁺-Ca²⁺ exchange in the heart: allosteric activation, spatial localization, sparks and excitation-contraction coupling

Lulu Chu¹, Joseph L. Greenstein¹, and Raimond L. Winslow^{1,†}

¹Department of Biomedical Engineering and the Institute for Computational Medicine, The Johns Hopkins University School of Medicine and Whiting School of Engineering, 3400 N Charles Street, Baltimore MD, 21218, USA

Abstract

The cardiac sodium (Na⁺)/calcium (Ca²⁺) exchanger (NCX1) is an electrogenic membrane transporter that regulates Ca²⁺ homeostasis in cardiomyocytes, serving mainly to extrude Ca²⁺ during diastole. The direction of Ca²⁺ transport reverses at membrane potentials near that of the action potential plateau, generating an influx of Ca²⁺ into the cell. Therefore, there has been great interest in the possible roles of NCX1 in cardiac Ca²⁺-induced Ca²⁺ release (CICR). Interest has been reinvigorated by a recent super-resolution optical imaging study suggesting that ~18% of NCX1 co-localize with ryanodine receptor (RyR2) clusters, and ~30% of additional NCX1 are localized to within ~120 nm of the nearest RyR2. NCX1 may therefore occupy a privileged position in which to modulate CICR. To examine this question, we have developed a mechanistic biophysically-detailed model of NCX1 that describes both NCX1 transport kinetics and Ca²⁺-dependent allosteric regulation. This NCX1 model was incorporated into a previously developed super-resolution model of the Ca²⁺ spark as well as a computational model of the cardiac ventricular myocyte that includes a detailed description of CICR with stochastic gating of L-type Ca²⁺ channels and RyR2s, and that accounts for local Ca²⁺ gradients near the dyad via inclusion of a peri-dyadic (PD) compartment. Both models predict that increasing the fraction of NCX1 in the dyad and PD decreases spark frequency, fidelity, and diastolic Ca²⁺ levels. Spark amplitude and duration are less sensitive to NCX1 spatial redistribution. On the other hand, NCX1 plays an important role in promoting Ca²⁺ entry into the dyad, and hence contributing to the trigger for RyR2 release at depolarized membrane potentials and in the presence of elevated local Na⁺ concentration. Whole-cell simulation of NCX1 tail currents are consistent with the finding that a relatively high fraction of NCX1 (~45%) resides in the dyadic and PD spaces, with a dyad-to-PD ratio of roughly 1:2. Allosteric Ca²⁺ activation of NCX1 helps to “functionally localize” exchanger activity to the dyad and PD by reducing exchanger activity in the cytosol thereby protecting the cell from excessive loss of Ca²⁺ during diastole.

[†]To whom correspondence should be addressed: rwinslow@jhu.edu.

Publisher's Disclaimer: This is a PDF file of an unedited manuscript that has been accepted for publication. As a service to our customers we are providing this early version of the manuscript. The manuscript will undergo copyediting, typesetting, and review of the resulting proof before it is published in its final citable form. Please note that during the production process errors may be discovered which could affect the content, and all legal disclaimers that apply to the journal pertain.

Keywords

cardiac myocyte; sodium-calcium exchanger; calcium micro-domains; calcium sparks; spark rate; spark fidelity; computational model

Introduction

The cardiac sodium (Na^+)-calcium (Ca^{2+}) exchanger (NCX1) is an antiporter membrane protein which transports three Na^+ ions across the sarcolemma in exchange for counter-transport of a single Ca^{2+} ion. Trans-sarcolemmal Na^+ and Ca^{2+} concentration gradients and membrane potential (V_m) determine whether NCX1 functions in the forward mode (Ca^{2+} efflux, inward net current) or reverse mode (Ca^{2+} influx, outward net current). NCX1 plays a key role in the regulation of intracellular $[\text{Ca}^{2+}]_i$ and $[\text{Na}^+]_i$ in cardiomyocytes, serving as the primary Ca^{2+} extrusion mechanism. In larger mammals, NCX1 extrudes ~ 20–50% of the total Ca^{2+} comprising the intracellular Ca^{2+} transient [1, 2], matching the amount of Ca^{2+} that enters through L-type Ca^{2+} channels (LCCs) at steady state. However, as a complex nexus integrating both Ca^{2+} and V_m signals, there remain gaps in our understanding of the multiple physiological roles of NCX1 in cardiac function in health and disease.

Elevation of intracellular Ca^{2+} concentration ($[\text{Ca}^{2+}]_i$) allosterically activates NCX1 allowing ionic exchange to occur. The thermodynamically driven cycling of NCX1 as well as its allosteric activation are Ca^{2+} -dependent mechanisms, therefore these underlying processes can be difficult to differentiate experimentally. Allosteric regulation of NCX1 by $[\text{Ca}^{2+}]_i$ was originally demonstrated in mammalian cells by Kimura et al. [3] via two high-affinity Ca^{2+} ion binding sites. These sites are distinct from the ion transport sites, and exhibit high cooperativity of binding [4]. More recently it has been shown that there are two Ca^{2+} binding domains (CBD1 and CBD2; jointly termed CBD12) that bind up to six Ca^{2+} ions per protein [5–8]. CBD1 and CBD2 contain four (Ca1, Ca2, Ca3, and Ca4) and two (CaI and CaII) Ca^{2+} -binding sites, respectively [5, 9]. Measurements of Ca^{2+} binding affinities in isolated CBD12 proteins in vitro [7] and analyses of transporter currents in NCX1 mutants with each Ca^{2+} binding site ablated have helped identify their regulatory roles [5, 10, 11]. These studies indicated that at low $[\text{Ca}^{2+}]_i$ the two high affinity sites of CBD1, Ca3 and Ca4, act as the primary Ca^{2+} sensors [10]. Elevated $[\text{Ca}^{2+}]_i$ may result in occupation of the CaI site at CBD2 [5, 12], further activating NCX1. The low affinity sites of CBD1, Ca1 and Ca2, and CBD2 site CaII are likely to be occupied only at very high $[\text{Ca}^{2+}]_i$, as would occur in the dyadic space between the opposing membranes of the t-tubules and the junctional sarcoplasmic reticulum (JSR) in cardiomyocytes [13]. Time constants of allosteric NCX1 activation have been measured in the range of 0.1–10 s in membrane patches [10, 14–17] and additional studies using caffeine application [18–20] or flash-photolysis [21, 22] to generate rapid elevation of $[\text{Ca}^{2+}]_i$ demonstrated rapid activation of NCX1 by $[\text{Ca}^{2+}]_i$. The Ca^{2+} half-activation concentration ($K_{m\text{Act}}$) has been measured in the range of 25–600 nM in both membrane patches and intact cardiomyocytes [17, 18, 23–26]. Ottolia et al. [27] observed beat-to-beat conformational changes in CBD12 by measuring fluorescent resonance energy transfer in response to changes of $[\text{Ca}^{2+}]_i$ in cardiomyocytes, but how these changes in CBD12 conformation lead to NCX1 activation remains unclear.

These data suggest that allosteric regulation of NCX1 may occur over a wide range of $[Ca^{2+}]$ from as low as ~ 100 nM to as high as ~ 100 μ M. Therefore, the spatial distribution and localization of NCX1 will be an important factor in determining the nature of its Ca^{2+} -dependent allosteric regulation. If positioned in or near the dyad, NCX1 can potentially be strongly activated by high (> 100 μ M) local $[Ca^{2+}]$ in the dyadic space ($[Ca^{2+}]_d$). While multiple immunofluorescence labeling studies have suggested that up to 40–60% of NCX1 is localized in the t-tubular system [28–33], it has been difficult to assess the degree to which NCX1 is co-localized within and/or near the dyad in imaging studies because of the high spatial resolution required to address this question. Early studies [28, 30] showed that only 4–8% of NCX1s are co-localized with type 2 ryanodine receptors (RyR2s) in rat myocytes. However, using immuno-gold labeling methods, Thomas et al. [31] estimated that the distribution of NCX1s and RyR2s were similar. This debate has been re-invigorated by a recent study in which super-high resolution optical imaging showed that $\sim 18\%$ of NCX1s co-localize (i.e., fluorescent labels targeted to NCX1 and RyR2 share overlapping voxels) with RyR2s in the dyad, and that $\sim 30\%$ of additional NCX1s are within 120 nm of the nearest RyR2 [34]. These important new findings suggest that NCX1 may be in a privileged location to modulate cardiac Ca^{2+} -induced Ca^{2+} -release (CICR).

Experimental studies suggest that NCX1 may play multiple roles in CICR. Several studies employing NCX1 inhibition or de-tubulation have demonstrated that forward mode NCX1-mediated Ca^{2+} extrusion may lower whole-cell Ca^{2+} spark frequency and Ca^{2+} spark amplitude [34–37]. There has been significant debate as to whether or not NCX1 current reverses during the action potential (AP) and generates an influx of Ca^{2+} that contributes to the trigger for JSR Ca^{2+} release. Some studies have shown no role of reverse-mode NCX1-mediated Ca^{2+} entry on CICR [38–40]. Others have demonstrated increased Ca^{2+} triggering currents or augmented Ca^{2+} release at depolarized potentials attributable to reverse-mode NCX1 Ca^{2+} flux [41–45]. It has been suggested that voltage-dependent LCC openings following the AP upstroke provide Ca^{2+} for allosteric NCX1 activation, which in turn allows NCX1-mediated Ca^{2+} influx to enhance CICR during the AP plateau [44].

These results demonstrate how challenging it can be to experimentally tease apart the complex role of NCX1 in CICR. To help address this question, this study presents a new biophysically based computational model of NCX1 describing both its transport kinetics and allosteric regulation by Ca^{2+} . This model of NCX1 is integrated into a previously developed three-dimensional (3D) model of the Ca^{2+} spark that includes high spatial resolution representations of the JSR, T-tubules, and the dyadic space [46], referred to as the super-resolution spark (SRS) model. The SRS model is used to investigate how positioning NCX1 at specific locations within and near the dyad influences Ca^{2+} spark generation. Furthermore, the Greenstein and Winslow model of the cardiac ventricular myocyte [47], which reproduces independent (stochastic) local dyadic JSR Ca^{2+} release events underlying cell-wide excitation-contraction coupling (ECC), is extended to incorporate a spatial “peri-dyad” (PD) compartment that is immediately adjacent to and surrounding each dyad. The parameters that define Ca^{2+} fluxes both into and out of the PD, and hence PD Ca^{2+} concentration ($[Ca^{2+}]_{pd}$), are informed by the SRS model results in order to ensure validity of this multi-scale modeling approach. This whole-cell model is used to examine the ways in

which differential placement of NCX1 into cytosolic, PD, and dyadic compartments influences properties of CICR and the cardiac AP.

Using the SRS and whole-cell models it is demonstrated that in diastole, both dyad and PD NCX1 can modulate spark fidelity, spark rate, and diastolic $[Ca^{2+}]_d$ to a degree that depends upon NCX1 density. However during a spark, the presence of dyad and/or PD NCX1 has little effect on spark duration and peak $[Ca^{2+}]_d$. Redistribution of NCX1s from the cytosol to the dyad or PD shortens the time to reversal of NCX1 current (I_{NCX1}) and greatly influences AP morphology by depolarizing the AP notch and prolonging AP duration (APD). NCX1 can play an important role in promoting Ca^{2+} entry into the dyad, and hence contributing to the trigger for JSR Ca^{2+} release at depolarized membrane potentials (>30 mV) with 10 mM intracellular Na^+ concentration ($[Na^+]_i$); however, immediately following the AP upstroke, the short-lived outward mode of I_{NCX1} limits Ca^{2+} entry and is insufficient to allow NCX1 to contribute significantly to CICR. Interestingly, the simulations show that elevated local intracellular Na^+ concentration in the dyad and peri-dyad space ($[Na^+]_d$ and $[Na^+]_{pd}$) further facilitates Ca^{2+} entry via NCX1 upon AP upstroke and enhances RyR2 open probability, which amplifies the NCX1 contribution to CICR. In addition, the whole-cell model predicts how differential placement of NCX1 into cytosolic, PD, and dyadic compartments affects the morphology of whole-cell I_{NCX1} (under AP clamp), with the best reproduction of experimental data achieved for an NCX1 distribution that matches the recent imaging data of Wang et al. [34], with a dyad-to-PD NCX1 placement ratio of $\sim 1:2$. Finally, allosteric Ca^{2+} activation of NCX1 helps to “functionally localize” exchanger activity to the dyad and PD by reducing exchanger activity in the cytosol, thereby protecting the cell from excessive loss of Ca^{2+} during diastole which would adversely affect Ca^{2+} spark generation and CICR.

Methods

NCX1 kinetic model with CBD12-mediated allosteric activation

The NCX1 current model consists of two modules. The first, shown in Fig. 1A, describes NCX1 electrochemical transport kinetics. The second, shown in Fig. 1B, describes Ca^{2+} -dependent allosteric regulation. NCX1 current is the product of an electrochemical factor (E) and an allosteric factor ($Allo$), as shown in previous studies [18, 48]:

$$I_{NCX1} = Allo \times \Delta E \quad (1)$$

E represents the transport of Na^+ and Ca^{2+} across the cell membrane and is modeled as a Markov process representation of the ping pong bi bi cyclic reaction scheme [49, 50], which is a consecutive ordered kinetic mechanism that has two membrane-crossing transitions. NCX1 is assumed to function at a non-equilibrium steady state and the turnover rate is represented using the net reaction velocity through the NCX1 cycle. The governing equations for ion transport are developed in the Supporting Material (Eqs. S2–S14). The rates for membrane translocation reflect the rate-limiting steps of NCX1 cycling, which are dependent on V_m and the unloaded exchanger charge ($\sim -2.56e$) [22, 51], as described by Keener and Sneyd [52]. The ion binding/dissociation rate constants and membrane translocation rate constants in the NCX1 transport model were constrained utilizing

experimental steady state NCX1 current-voltage (I-V) curves measured using fully-active NCX1 in giant membrane patches [14] (Fig. S2).

Allosteric regulation of NCX1 is mediated via Ca^{2+} binding to the CBD12 domain [13, 27]. A sequential binding CBD12 model consisting of a linear set of seven states ($A_0 - A_6$) was first developed using data on the binding affinities for each site measured in isolated CBD12 proteins [7, 53]. The association and dissociation rate constants were determined by fitting experimental measurements of the CBD12 equilibrium Ca^{2+} binding curve as well as data from kinetic stop-flow experiments of Ca^{2+} dissociation (Fig. S4A–B). The detailed simplification of the CBD12 model is given in the Supplement (Supplemental Methods 1.2 CBD12). Figure 2A shows that the equilibrium Ca^{2+} binding curve for the simplified model reproduces experimental data [7].

In response to a rapid increase in $[\text{Ca}^{2+}]_i$, I_{NCX1} exhibits an initial nearly instantaneous increase (reaching ~80% of peak I_{NCX1} magnitude in less than 500 ms) followed by a small secondary slow activation phase ($\tau = 2-5$ s) [24]. Therefore, as shown in Fig. 1B, it was assumed that Ca^{2+} -bound NCX1s transition through two conformational states when becoming activated (fast transition to A_{2c} or A_{46c} , slower transition to A_{2cc} or A_{46cc}). A partial activity coefficient $F(\text{state})$ is assigned to each activated state to represent fractional activity of NCX1 in that state (Fig. 1B, red values), and the weighted sum of the CBD12 state activities represents the total allosteric activity of NCX1 as follows:

$$Allo = F_{2c}A_{2c} + F_{2cc}A_{2cc} + F_{46c}A_{46c} + F_{46cc}A_{46cc} \quad (2)$$

Conformational rate constants and partial activity coefficients were optimized to reproduce measurements of peak NCX1 activities (Fig. S5A) [15, 24] and properties of NCX1 Ca^{2+} -dependent allosteric activation upon a step increase in $[\text{Ca}^{2+}]$ (Fig. S5B) [24]. $K_{m\text{Act}}$ is estimated to be ~300 nM, consistent with experimental measurements in inside-out membrane patches and whole-cell patch clamp studies [15, 23, 25, 26]. The allosteric regulation model shows that there are always 2 Ca^{2+} ions bound to the CBD12 protein at physiological resting $[\text{Ca}^{2+}]$ (~100 nM), and there is a baseline NCX1 fractional activity of ~0.3.

The NCX1 model was then validated by comparison with experimental data not included in the parameter fitting process. The model reproduced experimental measurements of NCX1 fractional activity [17], steady state wild-type I_{NCX1} [54], and dynamics of Ca^{2+} -dependent activation [17], as shown in Fig. 2B–D. The fractional activity of CBD12 saturates at $[\text{Ca}^{2+}]$ above ~30 μM , suggesting that its function remains sensitive to high levels of Ca^{2+} as predicted to occur in and near the dyad. A rapid increase in $[\text{Ca}^{2+}]_i$ results in rapid activation of NCX1 current, followed by a slow secondary phase (Fig. 2D), which is qualitatively similar to NCX1 Ca^{2+} activation dynamics measured in response to a step increase of $[\text{Ca}^{2+}]$ reported by Fujioka et al. [17]. The model exhibits relatively slow activation kinetics in response to moderate $[\text{Ca}^{2+}]$ steps, as would be sensed in the cytosolic compartment (Fig. S7A–C), but the kinetic response of the exchanger is rapid in response to high $[\text{Ca}^{2+}]$, as would be sensed within and near the dyad (Fig. S7D–F). To further investigate NCX1

behavior with Ca^{2+} allosteric regulation intact, additional Ca^{2+} clamps as well as Ca^{2+} signals simulated during AP pacing in the Greenstein and Winslow model [47] were applied as inputs to this NCX1 model.

NCX1 in the super-resolution spark model

Walker et al. [46] recently developed the super-resolution spark (SRS) model in rat. This model was used here to explore the potential roles of NCX1 in the dyadic space and nearby regions. In the SRS model, the area of JSR membrane in contact with the t-tubule is assumed to be a square with 465 nm edge length that wraps around a t-tubule, as shown in Fig. 1C–D. A 7×7 lattice of RyR2s is positioned in the center of the JSR dyadic surface. In order to facilitate comparison of SRS model spark properties in rat with those obtained in the whole-cell model [47] used here, it was necessary to reduce spark frequency from that measured in rat to that measured in canine. The ratio of spark frequency in rat versus canine is ~ 2.3 ($\sim 133 \text{ cell}^{-1} \text{ s}^{-1}$ in rat vs. $\sim 59 \text{ cell}^{-1} \text{ s}^{-1}$ in canine at $1 \text{ mM JSR } [\text{Ca}^{2+}]$ ($[\text{Ca}^{2+}]_{\text{JSR}}$) [55, 56]. The RyR2 opening rate in the SRS model was adjusted to reproduce lower Ca^{2+} spark rate measured in canine versus rat. At rest, the adjusted canine whole-cell model produces a spark rate of $\sim 1.3 \text{ cell}^{-1} \text{ s}^{-1}$ with $700 \mu\text{M } [\text{Ca}^{2+}]_{\text{JSR}}$.

As shown in Fig. 1D (red shaded region), the region bounded by the lateral edge of the JSR and the outer edge of the centrally-located RyR2 lattice is defined as the peri-dyad (PD). The profile of $[\text{Ca}^{2+}]$ declines very rapidly with distance outside this region, becoming comparable to $[\text{Ca}^{2+}]_i$ [57]. The model PD extends 124 nm beyond the RyR2 cluster, and has a height of 15 nm. Model simulations predict the average Ca^{2+} in this region is greatly elevated compared to $[\text{Ca}^{2+}]_i$, with a peak of $\sim 70 \mu\text{M}$ during a Ca^{2+} spark (Fig. S6D). Approximately 30% of non-dyadic NCX1s have been estimated to be within 120 nm of the nearest RyR2 in the recent imaging study of Wang et al. [34] (values estimated from their Fig. 5D).

NCX1s are treated as Ca^{2+} point sources arranged in the t-tubule membrane on a lattice with 31 nm spacing (opposite RyR2s). To examine the effects of local I_{NCX1} on Ca^{2+} spark properties and spark fidelity (i.e. the probability that a spontaneous RyR2 opening triggers a Ca^{2+} spark), V_m was fixed at -80 mV and either the central or a randomly selected RyR2 was opened. The spark rate (per release site) was determined by the product of spark fidelity and RyR2 opening rate, and was then scaled to per cell values. NCX1s were positioned only within the dyad and/or PD at various membrane densities, and the effect of this positioning on Ca^{2+} sparks was investigated. Since RyR2s and NCX1s gate stochastically, more than 1,000 simulations were performed for each choice of NCX1 spatial distribution, and average responses were calculated. The methods used to estimate Ca^{2+} spark fidelity and rate are those previously described by Walker et al. [46].

Spatial localization of NCX1 in the canine whole-cell model

In order to evaluate the roles of NCX1 and its spatial localization on whole myocyte physiology, the NCX1 model was incorporated into the Greenstein and Winslow [47] model of the canine ventricular myocyte, which incorporates stochastic simulations of LCC and RyR2 gating. In this model, the t-tubule-JSR cleft is represented as a four-compartment dyad

(in which a single dyadic compartment is referred to as a subspace) surrounded by a single PD compartment (Fig. 1E), which taken together with their associated LCCs and RyR2s, is referred to as a Ca^{2+} release unit (CRU). Ca^{2+} concentration is assumed to be uniform within each compartment, and Ca^{2+} may diffuse passively between adjacent subspace compartments or across a subspace-PD boundary within the same CRU. Each dyadic subspace contains 2 LCCs and 12 RyR2s in the t-tubule and the JSR membranes, respectively (consistent with the SRS model). This yields a total of 8 LCCs and 48 RyR2s per CRU. A total of 6250 active CRUs were included per myocyte to give a total of 50,000 active LCCs, the ensemble current of which correspond to whole-cell measurements in canine myocytes [58]. A subset of CRUs (625 or 10%) was used for all simulations in this study and all CRU Ca^{2+} fluxes were scaled to the total number of CRUs to obtain whole-cell spark rate or whole-cell LCC currents and RyR2 Ca^{2+} fluxes. In addition, the whole-cell model was updated to incorporate the same 2-state RyR2 model [59] as that used in the SRS model. Ca^{2+} -dependent allosteric regulation of NCX1 in the dyad and PD was simulated stochastically while the thermodynamically driven NCX1 transport rate was assumed to operate in steady-state at all times.

As shown in Fig. 1E, the whole-cell model was extended such that each CRU includes a single PD compartment immediately adjacent to and surrounding the dyad which is a simplified representation of the PD space modeled in the SRS model. The volume of the PD is $\sim 4\times$ that of the dyad, matching the SRS model PD volume. The PD is a single compartment with uniform Ca^{2+} concentration ($[\text{Ca}^{2+}]_{\text{pd}}$), and Ca^{2+} can diffuse between it, the cytosol, and each of the dyad subspace compartments. The PD model is defined by two parameters; the Ca^{2+} diffusion (transfer) rate between a CRU subspace and the PD (r_{sp2pd}); and the diffusion rate between the PD and cytosol (r_{pd2c}). These two parameters were constrained to match SRS model PD Ca^{2+} profiles and average spark properties under resting conditions (Fig. S6). These steps were taken in order to ensure that the parameters that determine the nature of Ca^{2+} fluxes both into and out of the PD, and hence $[\text{Ca}^{2+}]_{\text{pd}}$, are informed by the well-constrained SRS model results [46]. This is a critically important step in this multi-scale approach and enhances the validity of the whole-cell model predictions. Spontaneous sparks were measured in the whole-cell model with V_m held at -80 mV for 20 s and the simulated CRU release events were analyzed and used to estimate spark rate. A spark was determined to have occurred if the $[\text{Ca}^{2+}]$ peak magnitude in a single dyadic subspace exceeded a threshold of 100 μM .

In order to explore the physiological roles of Ca^{2+} -dependent allosteric regulation of NCX1 and the effects of NCX1 localization on ECC, NCX1 was positioned with various distributions among the dyadic, PD, and cytosolic Ca^{2+} compartments of the cell and both ECC gain and AP pacing protocols were performed. The distribution of NCX1 in the whole-cell model is defined by three parameters, f_d , f_{pd} , and f_{cyto} , which represent the fraction of NCX1s that are localized to dyads, PDs, and the cytosol, respectively. By definition $f_d + f_{\text{pd}} + f_{\text{cyto}} = 1$, and for notational convenience the combined fraction of NCX1s localized to both dyad and PD is denoted $f_{\text{d+pd}} = f_d + f_{\text{pd}}$. APs were generated by pacing at 1 Hz for 15 – 20 beats until cytosolic Ca^{2+} transients reached steady state. $[\text{Na}^+]_i$ is clamped to 10 mM for all simulations in Figures 3–9.

Results

I_{NCX1} driven by $[\text{Ca}^{2+}]_{\text{d}}$ and $[\text{Ca}^{2+}]_{\text{i}}$

In order to investigate dynamics of NCX1 Ca^{2+} -dependent allosteric regulation in response to physiologically relevant $[\text{Ca}^{2+}]$ during the AP clamp, template V_{m} (Fig. 3A), $[\text{Ca}^{2+}]_{\text{i}}$ (Fig. 3B, black line), and $[\text{Ca}^{2+}]_{\text{d}}$ (Fig. 3B, red line) waveforms were generated using a previous whole-cell model [60]. The model was paced for at 1 Hz starting from rest and these signals were then used to drive the NCX1 model presented here. Figure 3C displays the NCX1 allosteric factor ($Allo$), and Fig. 3D shows I_{NCX1} . Driving NCX1 beat-to-beat with the higher $[\text{Ca}^{2+}]_{\text{d}}$, as compared to $[\text{Ca}^{2+}]_{\text{i}}$, leads to a relatively more rapid allosteric activation of the exchanger and a greater level of NCX1 CBD12 activity is achieved. Similar simulation results are achieved in response to step increases of $[\text{Ca}^{2+}]$ in conjunction with voltage-clamp (Fig. S7). I_{NCX1} exhibits dramatically different responses to dyadic and cytosolic Ca^{2+} signals underlying the APs starting from the 1st beat. NCX1 current driven by $[\text{Ca}^{2+}]_{\text{i}}$ is primarily outward during the first ~200 ms of the AP. On the other hand, the NCX1 current driven by $[\text{Ca}^{2+}]_{\text{d}}$ exhibits a very brief outward current after the AP upstroke immediately followed by a rather large inward current arising from the elevation of $[\text{Ca}^{2+}]_{\text{d}}$ and the current remains inward for the remainder of the AP.

Effect of NCX1 on Ca^{2+} sparks in the SRS model

To explore effects of NCX1 placement on spark morphology and frequency, NCX1s were positioned in the dyad, PD, or both within the SRS model. The dyadic area of the t-tubule in this model is defined as a square patch of membrane directly opposed to the 7×7 array of RyR2s in the JSR membrane. This sarcolemmal membrane patch is similarly subdivided into a 7×7 array (where each element is $31 \text{ nm} \times 31 \text{ nm}$) such that NCX1s can be placed directly across the cleft from RyR2s. The t-tubule surface of the PD is defined by a concentric 15×15 array of similar membrane lattice elements excluding the central 7×7 array (which are within the dyad), on which NCX1s can be placed. To vary NCX1 membrane density, increasing numbers of NCX1 transporters (0 – 3) were allocated to the sarcolemmal membrane lattice sites within the dyad and/or PD. A spark was initiated by opening a random RyR2 in the dyad (Fig. 4). Figure 4A plots Ca^{2+} spark fidelity as a function of NCX1 membrane density when NCX1s are placed only in the dyad (blue bars), only in the PD (red bars), or in both dyad and PD (dyad + PD, yellow bars) under resting conditions. Spark fidelity decreases as NCX1 membrane density increases in all three cases. Exchangers placed in the dyad have a greater impact on spark fidelity reduction than those placed in the PD. The model predicts a ~ 32% reduction in spark fidelity when placing 2 NCX1s opposite each RyR2 in the dyad compared to the baseline case with no NCX1. Placement of NCX1 in dyad + PD, compared with placement in the dyad alone, further contributes to the reduction of spark fidelity, however the PD NCX1s only weakly influence local Ca^{2+} spark generation. An increasing presence of NCX1 in the dyad and/or PD reduced spark rate (Fig. 4B), which is qualitatively consistent with experiments showing that NCX1 inhibition or de-tubulation leads to an increased spark rate [34, 35, 37]. Mean values of peak $[\text{Ca}^{2+}]_{\text{d}}$ (Fig. 4C) decrease with increasing density of NCX1 positioned in the dyad, PD, or both. The mean Ca^{2+} spark amplitude is not significantly different from control (no NCX1) when only 2 or fewer NCX1s are placed across each RyR2 in the dyad, however

with 3 NCX1s placed at each sarcolemmal lattice site, there is a small but significant reduction in spark amplitude of ~ 20% ($p < 0.05$) compared to control (Fig. 4C). These simulations support the idea that lower levels of dyadic NCX1 do not have a significant effect on Ca^{2+} spark amplitude, but can effectively regulate spark fidelity and rate. The former conclusion is in agreement with Hake et al. [61] who concluded that NCX1 has minimal impact on $[\text{Ca}^{2+}]_d$ once JSR Ca^{2+} release is initiated due to the fact that NCX1 Ca^{2+} flux is quite small relative to the RyR2 Ca^{2+} release flux. With 1 mM $[\text{Ca}^{2+}]_{\text{jsr}}$ and 100 nM $[\text{Ca}^{2+}]_d$, a single NCX1 current is calculated to be $\sim 7.2 \times 10^{-7}$ pA, which is at least 100,000 times smaller than a unitary RyR2 Ca^{2+} current (9.77×10^{-2} pA). At 100 μM $[\text{Ca}^{2+}]_d$ (comparable to Ca^{2+} spark amplitude), a single NCX1 current is estimated to be $\sim 2 \times 10^{-4}$ pA, consistent with experimentally measured maximum unitary NCX1 current [62] but still dwarfed by unitary RyR2 current. Therefore it is not surprising that even when positioned in the dyad, NCX1 has little effect on Ca^{2+} release following spark initiation. However, at higher dyadic NCX1 densities (> 3 exchangers per lattice element) which are physiologically less likely to occur, there is a smaller Ca^{2+} gradient between JSR and dyad, and the NCX1 Ca^{2+} flux becomes comparable to Ca^{2+} flux through a single open RyR2, and therefore reduces Ca^{2+} spark amplitude (Fig. S8). The reason this is physiologically unlikely is that these higher densities correspond to a localization of $>50\%$ of the cell NCX1 to the dyad, which is greater than the upper bound observed in NCX1-RyR2 co-localization imaging studies [28, 29, 34]. Based on the observation that ~18% of NCX1 co-localize with RyR2 clusters [34], ~70 exchangers are calculated to reside in each dyad, which corresponds to 1–2 NCX1s per sarcolemmal lattice element. In contrast, NCX1s placed in the PD are by definition displaced from the dyad and therefore have less of impact on spark properties and $[\text{Ca}^{2+}]_d$. NCX1 placement in the dyad and/or PD leads to minor reductions in spark duration (measured as full duration at half maximum amplitude, FDHM) (Fig. 4D) which is in qualitative agreement with experimental findings [34, 36]. These results show that spark fidelity and rate are most strongly affected by dyadic and PD placement of NCX1, while effects on spark amplitude and duration are less significant. Simulations in which the spark was initiated by the center RyR2 (Fig. S9) yielded similar results on NCX1-mediated modulation of spark fidelity, rate, and morphology.

Role of NCX1 localization on Ca^{2+} sparks in the whole-cell model

As mentioned earlier, the SRS model was used to guide the whole cell model building and parameter fitting to achieve consistency in whole cell spark frequency between the two models ($\sim 60 \text{ cell}^{-1}\text{s}^{-1}$). In order to understand the effects of NCX1 localization on Ca^{2+} spark properties and CICR at the whole-cell level, a variety of NCX1 distributions were analyzed. In the first case, NCX1 was assumed to reside only in the dyad or cytosol, but not in the PD (i.e. $f_{d+pd} = f_d = 1 - f_{\text{cyto}}$ since $f_{pd} = 0$) (Fig. 5, solid lines). In the second case, NCX1 was assumed to reside only in the PD or cytosol, but not in the dyad (i.e. $f_{d+pd} = f_{pd} = 1 - f_{\text{cyto}}$ since $f_d = 0$) (Fig. 5, dashed lines). Finally, NCX1 was assumed to reside in all three locations with a $f_d:f_{pd}$ ratio of 1:2 as suggested by the imaging data of Wang et al. [34] (i.e. $f_{d+pd} = f_d + f_{pd} = 1 - f_{\text{cyto}}$ where $f_{pd} = 2f_d$) (Fig. 5, dotted lines). In all cases, the total number of NCX1s in the cell was conserved. The effect of these different NCX1 distributions on spark rate (Fig. 5A), peak $[\text{Ca}^{2+}]_d$ (Fig. 5B), spark duration (Fig. 5C), and average diastolic $[\text{Ca}^{2+}]_d$ (Fig. 5D) were simulated in the whole-cell model. The results of

redistributing NCX1 between the dyad and cytosol only (i.e. $f_{pd} = 0$) are consistent with those obtained using the SRS model in that NCX1-mediated extrusion of Ca^{2+} at rest reduces whole-cell spark rate (Fig. 5A, solid line). Simulations show that placing ~ 20% of NCX1 in the dyadic space (~ 80 % in cytosol) results in ~ 40% reduction in spark rate and by placing ~ 80% of NCX1 in the dyad (~ 20% in cytosol), spark activity is nearly eliminated. While spark rate is highly dependent on spatial distribution of NCX1, the whole-cell model shows that dyadic NCX1 plays less of a role in regulating individual Ca^{2+} spark properties, and that redistributing NCX1 to PD and cytosol only (i.e. $f_d = 0$) has much less impact on all spark properties (Fig. 5, dashed lines). Mean peak $[Ca^{2+}]_d$ and spark duration are reduced with increasing NCX1 distribution to the dyad and/or PD in a manner that matches the results of the SRS model. Furthermore, as predicted using the SRS model, spark duration is minimally influenced by redistribution of NCX1 to the dyad and/or PD (Fig. 5C). Diastolic $[Ca^{2+}]_d$ is greatly diminished with increasing NCX1 distribution to the dyad and/or PD in the whole-cell model (Fig. 5D) consistent with SRS model behavior (data not shown). This underlies the associated reduction on spark frequency and suggests the spatial distribution of NCX1 plays an important role in resting cellular Ca^{2+} homeostasis.

NCX1 localization and the cardiac action potential

APs were generated in the whole-cell model under various distributions of NCX1 between the cytosolic and dyadic compartments, with no NCX1 in the PD (f_d values of 0, 0.05, 0.10, 0.15, and 0.20, all with $f_{pd} = 0$) to examine underlying Ca^{2+} dynamics. The model was paced at 1 Hz to steady-state (15 beats) from the same initial condition for each NCX1 distribution. Simulation results from the final paced beat in Fig. 6A show that the AP notch becomes more depolarized from -20 mV to 0 mV, and APD prolongs with increasing dyadic NCX1 distribution. Figure 6B demonstrates that increased f_d greatly enhances forward mode NCX1 operation, which underlies the depolarization of the AP notch. With sufficient dyadic NCX1, I_{NCX1} will be transiently inward during JSR Ca^{2+} release, temporarily outward during the early AP plateau, and will finally reverse to inward later in the AP plateau. There are therefore multiple times during the AP at which V_m and the NCX1 reversal potential (E_{NCX1}) intersect. With increasing f_d , the late phase of I_{NCX1} becomes increasingly inward, which shifts the NCX1 time-to-reversal from ~ 270 ms to ~ 150 ms and helps to prolong APD. NCX1 localization has minimal impact on $[Ca^{2+}]_{jsr}$ (Fig. 6C) and $[Ca^{2+}]_i$ (Fig. 6D). Fig. 6E illustrates average $[Ca^{2+}]_d$ during an AP whose peak is not significantly affected by redistribution of NCX1 to the dyad. Figure 6F displays the beginning of the diastolic phase of $[Ca^{2+}]_d$ following the decay of the Ca^{2+} transient where Ca^{2+} spark activity becomes more prevalent with fewer dyadic NCX1s (lower values of f_d). As f_d increases, NCX1 plays an increasing role in reducing the magnitude of $[Ca^{2+}]_d$ (Fig. 6E) and decreases diastolic spark rate (Fig. 6F). The corresponding time-courses of NCX1 equilibrium potential (E_{NCX1}) in the cytosol and dyad are illustrated in Fig. S10, and show that dyadic E_{NCX1} remains at a relatively high value (~ 40 mV) throughout the AP with NCX1 placement in dyad. Furthermore, redistribution of NCX1 from cytosol to dyad leads to a modest prolongation of the Ca^{2+} transient decay time constant from ~185 ms to ~215 ms (Table S4), and an increase in the fraction of cycled Ca^{2+} extruded from the cell by NCX1 on each beat from ~ 24% to ~ 36%. Redistribution of NCX1 between only cytosolic and PD compartments yields similar trends (Fig. S11 and Table S5). Interestingly, placement of

NCX1 in the PD has a stronger impact on $[Ca^{2+}]_i$ as compared to dyadic NCX1. With an $f_d:f_{pd}$ ratio of 1:2 (i.e., $f_d = 0.15$ and $f_{pd} = 0.3$), the Ca^{2+} transient decay time constant for 1 Hz AP pacing is quantified to be ~ 220 ms and NCX1 accounts for $\sim 36\%$ of Ca^{2+} extrusion during relaxation, which are both consistent with experimental measurements [2, 63, 64]. While these results clearly indicate that NCX1 plays an important role in extruding Ca^{2+} under physiological $[Na^+]_i$, it remains unclear whether the brief outward I_{NCX1} (Ca^{2+} influx) that occurs upon AP upstroke plays a role in triggering RyR2s and JSR Ca^{2+} release.

Does NCX1 play a role in CICR?

Whether NCX1 in the dyad can underlie a significant portion of the triggering current for CICR still remains controversial. In this model the NCX1 spatial distribution follows those identified in the imaging study of Wang et al. [34] (as calculated from their Fig. 5D) with f_d , f_{pd} , and f_{cyto} values of 0.15, 0.30, and 0.55, respectively. AP simulations at 1 Hz pacing show that the reverse mode of NCX1 which occurs upon AP upstroke precedes the onset of LCC trigger and RyR2 Ca^{2+} release (data not shown), which suggests a potential role for NCX1 in contributing to CICR. Therefore, the triggering role of reverse mode NCX1 was further investigated by application of voltage clamp protocols and comparison of control NCX1 Ca^{2+} flux (NCX1c, Fig. 7, black lines) to that in which only the reverse mode of I_{NCX1} was ablated by clamping it to zero (NCX1*, Fig. 7, red lines). The model was pre-conditioned with ten 200-ms depolarizations to 40 mV from a holding potential of -90 mV applied at 1 Hz to load JSR Ca^{2+} prior to application of a test potential (from -30 mV to 80 mV in 10 mV increments). The sum of dyad and PD NCX1 Ca^{2+} fluxes (J_{NCX1} , Fig. 7A), LCC Ca^{2+} flux (J_{LCC} , Fig. 7B), and RyR2 Ca^{2+} flux (J_{RyR2} , Fig. 7C) during the test potentials are shown for 0 mV and 50 mV test potentials for both the NCX1c and NCX1* cases. Since J_{NCX1} remains in forward mode (outward Ca^{2+} flux) during the entirety of the test potential at 0 mV, no difference is observed in the peaks of RyR2 Ca^{2+} flux between J_{NCX1c} and J_{NCX1*} . In contrast, the presence of inward J_{NCX1} in the dyad and PD can greatly augment RyR2 Ca^{2+} release at 50 mV while no apparent difference in peak J_{LCC} is detected (Fig. 7B, lower panel). The summary data showing peak CICR trigger Ca^{2+} influx in the presence ($J_{LCC} + J_{NCX1c}$, black line) or absence ($J_{LCC} + J_{NCX1*}$, red line) of reverse mode NCX1 are normalized and plotted in Fig. 7D and are consistent with experiments of Sobie et al. [44]. This result suggests that at more depolarized V_m (>30 mV), I_{NCX1} augments the Ca^{2+} trigger flux in CICR and can play an important role in triggering JSR Ca^{2+} release. Furthermore, the fractional contribution of NCX1 to the CICR trigger (i.e. $1 - J_{RyR2}(NCX1c)/J_{RyR2}(NCX1*)$) is shown in Fig. 7E. Reverse mode NCX1 contributes significantly to the CICR trigger at highly depolarized V_m , but does not contribute significantly when V_m is at more moderately depolarized potentials corresponding to the AP plateau. This is further confirmed by investigation of the role of reverse mode I_{NCX1} during AP pacing. During the AP upstroke, V_m briefly reaches >30 mV (lasting <5 ms), but for the remainder of the plateau phase it is closer to 0 mV. Blocking the reverse mode of NCX1 does not reduce the peak of J_{RyR2} (Fig. 7F) during the AP, which shows that NCX1 does not have a significant contribution to CICR under physiological $[Na^+]_i$, which is explained by limited NCX1-mediated Ca^{2+} entry during the brief AP upstroke.

Role of NCX1 localization on whole-cell I_{NCX1}

The AP clamp interruption protocols performed in the experiments of Weber et al. [54] were applied to the whole-cell model to examine the role of NCX1 localization on I_{NCX1} morphology. The model was pre-conditioned with ten 200 ms depolarizations to 40 mV applied at 1 Hz prior to the application of the AP-clamp. Each AP was interrupted at various times with a clamp to -90 mV to reveal NCX1 tail currents (LCCs are inactivated at -90 mV). Figure 8A displays the AP clamp used experimentally in a rabbit ventricular myocytes by Weber et al. [54] and that was used as an AP template in model simulations with AP interruptions at 10, 25, 50, 100, 200, and 300 ms following the pre-conditioning protocol. Figure 8B presents the NCX1 tail currents upon AP interruption from the original Greenstein and Winslow [47] model. The simulated NCX1 tail currents are smaller than the tail currents measured by Weber et al. [54] and exhibit a maximal peak at 200 ms. In addition, the decay of the current is slow. After updating the RyR2 formulation, incorporating the new PD compartment, and setting $f_{cyto} = 1.0$ (i.e. no NCX1 in dyad or PD), the simulated peak of NCX1 tail currents remains much smaller than those measured experimentally and the decay of current is faster (Fig. 8C). In contrast, with f_d , f_{pd} , and f_{cyto} values of 0.15, 0.30, and 0.55, respectively (Fig. 8D), I_{NCX1} tail currents more closely resemble those measured experimentally by Weber et al. [54] which displayed a maximal peak current for the 25 ms interrupted AP clamp (the approximate time of peak $[Ca^{2+}]_d$). These findings further support the idea that NCX1 is not localized solely to the cytosolic sarcolemma.

Role of NCX1 allosteric regulation on whole-cell physiology

The physiological role of beat-to-beat Ca^{2+} -dependent allosteric regulation of NCX1 was investigated with 1 Hz current clamp simulations at steady-state with f_d , f_{pd} , and f_{cyto} values of 0.15, 0.30, and 0.55, respectively (dyad-to-PD ratio of 1:2). The CBD12 model allows NCX1 allosteric activation to various levels of activity and enables NCX1 to play a local functional role in each subcellular compartment. Exchangers in the cytosol respond to a global Ca^{2+} signal, while those in the, PD, and dyad respond to a local Ca^{2+} signal. This results in differing levels of regulation (*Allo*) and I_{NCX1} behavior, as shown in Fig. 9A and 9B, respectively. In addition, the physiological role of NCX1 Ca^{2+} -dependent activation was further studied by removing the allosteric regulation (fully active NCX1, *Allo* = 1). Figure 9C displays a $\sim 40\%$ reduction in $[Ca^{2+}]_i$ with full NCX1 activity (red line) compared to control (blue line) and Fig. 9D shows a $\sim 15\%$ decrease in $[Ca^{2+}]_{jSR}$ in the absence of allosteric regulation. The control AP is illustrated in Fig. 9C. No significant difference is observed for APs as a result of removing the allosteric regulation (not shown). Full NCX1 activity associated with loss of NCX1 regulation facilitates Ca^{2+} extrusion during diastole resulting in a reduction of diastolic $[Ca^{2+}]_i$ (Fig. 9C) and $[Ca^{2+}]_d$ (not shown), and JSR Ca^{2+} load (Fig. 9D), which reduces resting Ca^{2+} spark generation and impacts efficiency of local CICR. These simulations demonstrate that the Ca^{2+} -dependent allosteric regulation of NCX1 is a means by which the myocyte can tune the activation of these exchangers in a spatially dependent manner. The ability of the cell to “functionally localize” NCX1 operation via this regulatory mechanism ensures proper function in each Ca^{2+} compartment. The partial deactivation of cytosolic NCX1 during diastole is important for maintaining normal cellular Ca^{2+} load and physiological Ca^{2+} transient properties.

Discussion

In this study, a biophysically based model of NCX1 incorporating allosteric regulation by Ca^{2+} is developed and analyzed. This NCX1 model captures properties of NCX1 allosteric regulation by Ca^{2+} over a wide range of $[\text{Ca}^{2+}]$ levels spanning from that in diastole (~ 100 nM) to those occurring at the peak of the dyadic Ca^{2+} transient (~ 100 μM or more). This improved model of NCX1 is incorporated into a super-resolution model of the Ca^{2+} spark that is based on realistic t-tubule and JSR geometry [46], as well as an integrative model of the cardiac ventricular myocyte in which L-type Ca^{2+} channels and RyR2s gate stochastically [47]. Parametric studies in both the SRS model and the whole-cell model demonstrate that localization of NCX1 to the dyad enables it to closely modulate the local $[\text{Ca}^{2+}]_d$, as well as Ca^{2+} spark fidelity and rate during diastole. Using a multi-scale approach, the whole-cell model is extended to incorporate a spatial PD compartment that is immediately adjacent to and surrounding each dyad, with parameters that define trans-PD Ca^{2+} fluxes informed by the SRS model results. This allows for the inclusion of NCX1s in various distributions within the PD and dyad compartments of each CRU. During AP pacing in the whole-cell model, this study shows that the dynamics of NCX1 activation depending on its localization to the cytosolic, PD, or dyadic compartments. Due to tight coupling between cellular Ca^{2+} cycling and V_m , along with the potential interaction of NCX1s with LCCs during CICR, it is difficult to experimentally control and study the L-type Ca^{2+} current and I_{NCX1} independently. Model simulations enable isolation of the functional effects of NCX1, and show that I_{NCX1} can act as a mechanism for additional Ca^{2+} entry and trigger JSR Ca^{2+} release at depolarized potentials (> 30 mV) in response to voltage-clamp steps. Model simulations qualitatively reproduce experimentally measured NCX1-mediated triggering of CICR [44] as well as NCX1 tail currents evoked by AP-clamp interruption protocols [54] when the NCX1 spatial distribution is adjusted to match the imaging results of Wang et al. [34], which showed that a high percentage of NCX1s reside in the dyad and PD with a dyad-to-PD ratio of roughly 1:2.

Spatial localization of NCX1

Optical imaging studies have quantified the co-localization between NCX1s and RyR2s in a wide range between 4% and 30% and have indicated 40–60% of NCX1s reside on the t-tubule membrane [28–34], which suggests that this localization is likely to be functionally important. In addition, inhibition of I_{NCX1} or NCX1 knockout in cardiomyocytes has been used to demonstrate the close proximity of NCX1 to RyR2 clusters and show the role of NCX1 in Ca^{2+} modulation at rest [34–37]. However, it remains difficult to differentiate NCX1 subpopulations which sense spatially-dependent differences in Ca^{2+} signals in intact cardiomyocytes. Several electrophysiology studies [54, 65, 66] in which NCX1 tail currents were measured during voltage- and/or AP-clamp indicated that the actual peak tail current is much larger than values calculated based on activation by $[\text{Ca}^{2+}]_i$ (i.e. assuming 100% NCX1 reside in the cytosol). Furthermore, during an AP, the NCX1 tail current peaks at ~ 25 ms, which suggests that NCX1 is rapidly activated upon RyR2 Ca^{2+} release and I_{NCX1} reflects the dynamics of $[\text{Ca}^{2+}]_d$ [54, 65, 66]. Despite these data, the spatial distribution of NCX1 within, near, and/or far from the dyads remained unclear. Recent super-resolution optical imaging, which demonstrated NCX1 localization within the dyad and the nearby

region, guided the distribution of NCX1 investigated in this model and simulation results are consistent with a number of experiments. The model simulations (Fig. 7D–E, Fig. 8B) adhering to a dyad-to-PD ratio of roughly 1:2 (f_d , f_{pd} , and f_{cyto} values of 0.15, 0.30, and 0.55, respectively) reproduce the ECC NCX1 triggering capacity experiments of Sobie et al. [44] and qualitatively match experimentally recorded NCX1 tail current magnitudes and time-to-peak during AP clamp [54]. These results provide additional evidence for the idea that a high percentage of NCX1s reside within or near the dyad consistent with a dyad-to-PD ratio of 1:2. Furthermore, three different NCX1 distributions with f_{d+pd} of 0.45 were evaluated for $[Ca^{2+}]_i$ transient rise-time (CRT). CRT gain was defined by Litwin et al. [41] as the maximum time rate of change of the Ca^{2+} transient divided by peak LCC current. Model simulations of the CRT gain (Fig. S12), where f_{d+pd} was redistributed between dyad and PD, show that with $f_d = 0.45$ and 10 mM $[Na^+]_i$, as f_d increases, CRT gain at depolarized membrane potentials increases compared to the 0 mM $[Na^+]_i$ case. However, the best reproduction of the relationship between CRT gain at 10 mM $[Na^+]_i$ vs. 0 mM $[Na^+]_i$ at highly depolarized membrane voltages (> 30 mV) as measured by Litwin et al. [41] was achieved for the case with dyad-to-PD ratio of 1:2 (Fig. S12).

Interspecies differences

Previous experimental data suggests that in small mammals (e.g. rats, mice), NCX1 is responsible for extruding only 7–10% of the total Ca^{2+} comprising intracellular Ca^{2+} transients, whereas in larger mammals (e.g. canine, guinea pig, rabbit), NCX1 extrudes 40–50% of the total Ca^{2+} [2, 64]. This interspecies difference in Ca^{2+} cycling could be attributed to species-dependent differences in NCX1 membrane density. Niggli & Lederer [22] calculated NCX1 membrane density of $\sim 250 \mu m^{-2}$ in mice, whereas Hilgemann et al. suggested 400–500 μm^{-2} in guinea pig cardiomyocyte [67]. NCX1 membrane density in this model can be adjusted to study interspecies differences. Another facet of species-dependent differences may be in the details of NCX1 spatial distribution. Additional super-resolution imaging studies are needed to quantify NCX1 placement in dyad, PD, and cytosol in a species-specific manner. Furthermore, the K_{mAct} s in Ca^{2+} -dependent allosteric activation can be species-dependent. This NCX1 model incorporates a Ca^{2+} -dependent allosteric activation mechanism which is closely based on CBD12 Ca^{2+} -binding studies in order to capture Ca^{2+} activation dynamics in the physiological range of $[Ca^{2+}]_i$. This NCX1 formulation responds over a wider dynamic range of Ca^{2+} signals than previous models, with a K_{mAct} of ~ 300 nM. Early experimental studies estimated NCX1 K_{mAct} to be in the range of 22–47 nM in guinea pig myocytes [23] or Chinese hamster ovary cells [68]. However, estimates of K_{mAct} in guinea-pig myocyte excised membrane patches or in expressed canine NCX1 measured at steady-state have been shown to be much lower, in the range of 200–800 nM [15, 24, 69–71]. More recent experiments using rapidly alternating Ca^{2+} influx-efflux voltage-clamp protocols in intact cardiomyocytes reported a K_{mAct} between in the range of 125–500 nM [18, 25, 26]. The K_{mAct} of this model agrees well with previous reports both in excised membrane patches and whole-cell voltage clamp recordings. In mouse, however, Ca^{2+} -dependent activation of NCX1 was not detected for $[Ca^{2+}]_i$ above 100 nM, therefore K_{mAct} has been suggested to be well below physiological diastolic $[Ca^{2+}]_i$ in this case [18]. This suggests the possibility that K_{mAct} is species-dependent and relevant parameters of the NCX1 model proposed here may need to be

adjusted for use in other species. However, additional experimental studies are needed to measure K_{mActS} in different animal species to guide further modeling studies.

The dual roles of NCX1

Spark fidelity is a measure of the probability that a single RyR2 opening leads to a spark and reflects properties of spontaneous spark generation in the absence of LCC activity at rest, whereas measures of ECC reflect excitability during LCC triggered CICR during an AP or voltage clamp stimulation. NCX1 may play different roles in these two different types of Ca^{2+} release events. Simulations with both the SRS and whole-cell models show that dyadic NCX1 plays an important role in extruding $[Ca^{2+}]_d$ at rest, thus effectively limiting Ca^{2+} accumulation and preventing local CICR and Ca^{2+} spark generation. Accordingly, a decrease in dyadic expression of NCX1 may result in enhanced Ca^{2+} spark activity. This may occur in the presence of down-regulation of the protein junctophilin-2 (JPH2), an anchor protein for RyR2s and possibly for NCX1s as well. Wang et al. [34] demonstrated that JPH2 knockdown reduces NCX1-RyR2 co-localization and functional I_{NCX1} (even without altered NCX1 protein expression), and this leads to increased JSR Ca^{2+} leak via increased resting Ca^{2+} spark activity. This was compared with pharmacological impairment of NCX1, which resulted in a qualitatively similar change in Ca^{2+} sparks. The result is further supported by Neco et al. [36] who demonstrated an increase in spark activity in NCX1 knockout mice compared to control. Moreover, a recent study has linked the down-regulation of JPH2 to potentially arrhythmic behavior by showing that mutant JPH2 mice exhibit a higher incidence of inducible atrial fibrillation than wild-type [57]. The reduction of NCX1-RyR2 co-localization in JPH2 mutants may be a contributing factor in these findings. The simulations reported here highlight the important role of dyadic NCX1 in regulating resting Ca^{2+} and its ultimate impact on local CICR in cardiac dyads.

While there is consensus regarding the important role of NCX1 for Ca^{2+} extrusion during diastole, the question still remains as to whether NCX1 cycling reverses and contributes to the trigger for CICR during an AP. Experimental and modeling studies have been unable to consistently identify whether NCX1 operates in forward or reverse mode during the AP plateau. The experiments of Grantham and Cannell [72] suggested that I_{NCX1} was predominantly outward (reverse mode) during an AP clamp, however I_{NCX1} was measured under an AP waveform with highly depolarized plateau (> 50 mV) and with JSR release minimized, a condition that promotes reverse mode operation of NCX. In contrast, duBell et al. [73] showed in rat myocytes that I_{NCX1} contributed to the net inward current that sustained the AP. Using a computational model of the guinea pig ventricular myocyte in which 100% of NCX1 was localized to the cytosol, Luo and Rudy [74] showed that I_{NCX1} becomes outward upon AP upstroke and this mode lasts ~ 100 ms before reversing to forward mode operation for the remainder of the AP and the diastolic inter-beat phase. On the other hand, in a computational model of the rabbit ventricular myocyte in which NCX1 senses subsarcolemmal $[Ca^{2+}]$, Weber et al. [54] predicted that the time of reversal of I_{NCX1} is very early in the AP (~ 19 ms) and that NCX1 operates in forward mode during the remainder of AP plateau. I_{NCX1} is highly sensitive to AP shape and $[Ca^{2+}]$ profiles of various subcellular compartments. Therefore variations in spatial distribution of NCX1 result in very different morphologies of the current as driven by an AP. Simulations of the

model presented here are consistent with the study of Sher et al. [75] which showed that NCX1 mainly works in forward mode to extrude Ca^{2+} during diastole, but functions in reverse mode transiently during the AP upstroke and the early part of the AP plateau phase.

Analysis of the direction of NCX1 during the AP naturally leads to the question of whether NCX1 impacts CICR. The whole-cell model simulation with reverse mode I_{NCX1} inhibited (NCX1*) revealed that NCX1 contributes to trigger Ca^{2+} entry (and subsequent JSR Ca^{2+} release) only under highly depolarized V_m (>30 mV), at 10 mM $[\text{Na}^+]_i$. Numerous studies have shown that $[\text{Na}^+]_i$ plays a crucial role in determining the transport direction of NCX1, which can alter the role of NCX1 in CICR. Recently, Na^+ currents have been shown to play a role in ECC. Specifically, Na^+ current block via either tetrodotoxin (TTX) or a pre-pulse inactivation protocol reduces JSR Ca^{2+} release flux in rabbit ventricular myocytes. This action is ablated in NCX1-knockout mice, supporting the hypothesis that Na^+ influx during the AP enhances reverse-mode NCX1 in a way that augments $[\text{Ca}^{2+}]_d$ in the vicinity of RyR2s [41, 76–78]. These results support the idea that a subpopulation of Na^+ channels (possibly neuronal) [77], reside within or near the dyad and can modulate ECC via local activation of NCX1 to prime $[\text{Ca}^{2+}]_d$ just prior to peak activation of LCCs and CICR. Localized domains of highly elevated $[\text{Na}^+]$ may form as t-tubular NCX1 and fast Na^+ channels introduce an influx of Na^+ in this confined space [79–81], and this can be a potent mechanism to drive reversal of I_{NCX1} , enhancing its contribution to the trigger for CICR. Therefore, microdomain $[\text{Na}^+]$ is likely to play an important role in modulating Ca^{2+} dynamics and CICR via the nexus that is NCX1.

Electron probe microanalysis has indicated that local $[\text{Na}^+]$ may reach ~ 40 mM within 20 nm of the inner side of the sarcolemma [82]. In order to investigate how $[\text{Na}^+]_d$ and $[\text{Na}^+]_{pd}$ affect CICR, we set $[\text{Na}^+]_d$ and $[\text{Na}^+]_{pd}$ to more elevated values than $[\text{Na}^+]_i$. Fig. S13A demonstrates that ECC gain increases at all membrane potential in response to an acute elevation of $[\text{Na}^+]_d$ and $[\text{Na}^+]_{pd}$ at the moment of depolarization (i.e. initial $[\text{Ca}^{2+}]_{jsr}$ and $[\text{Ca}^{2+}]_d$ are the same in all cases). In Fig. S13B, the Na^+ -dependent role of local NCX1 on $[\text{Ca}^{2+}]_d$ and $[\text{Ca}^{2+}]_{pd}$ during the pre-conditioning protocol remain intact and only the initial $[\text{Ca}^{2+}]_{jsr}$ is identical in all cases (see Supplement for details). In this case elevated $[\text{Na}^+]_d$ primes $[\text{Ca}^{2+}]_d$ via NCX1 which further amplifies the contribution of NCX1 to CICR. In addition, elevation of $[\text{Na}^+]_d$ and $[\text{Na}^+]_{pd}$ from 10 mM (black lines) to 40 mM for a short time period (10ms) beginning upon AP upstroke (red lines) or during the entirety of an AP-clamp (blue lines) leads to an amplified outward NCX1 current (Fig. S14A and S14B) with no observed difference in peak LCC fluxes. This results in a ~ 20–30% increase in SR Ca^{2+} release (Fig. S14C) and $[\text{Ca}^{2+}]_d$ (Fig. S14E), which is consistent with the experimental measurement of Ca^{2+} signal reduction upon TTX application observed by Torres et al. [77]. The reverse mode of NCX1 (Ca^{2+} -influx) preceding the peak of RyR2 release (10–20ms) is critical for increasing $[\text{Ca}^{2+}]_d$ (Fig. S14E), which sensitizes the RyR2s and enhances their open probability (Fig. S14 D). $[\text{Na}^+]_d$, through its influence on local NCX1, can therefore be a regulator of ECC. The impact of $[\text{Na}^+]_d$ on ECC saturates at levels above ~ 40 mM, suggesting that the relevant range in which $[\text{Na}^+]_d$ has functional impact is 10–40 mM, which is consistent with experimental estimates [82]. These findings indicate that further experimental studies of the role of local $[\text{Na}^+]$ in the regulation of CICR are needed.

Role of NCX1 Ca²⁺-dependent allosteric regulation

The beat-to-beat physiological role of NCX1 Ca²⁺-dependent allosteric regulation has long been debated and remains unclear. Weber et al. [83] originally suggested that, during an AP, allosteric regulation accelerates Ca²⁺ extrusion via NCX1 in response to the Ca²⁺ transient and as [Ca²⁺]_i approaches diastolic levels, NCX1 deactivates partially to limit diastolic Ca²⁺ extrusion. A recent study by Ginsburg et al. [48] suggested that deactivation is very slow (>10 s) such that the allosteric activity of NCX1 remains nearly constant from beat to beat during paced APs, but the degree of activation varies in a frequency-dependent manner. On the other hand, as a result of the high cooperativity of Ca²⁺ dependence in the model formulation (hill coefficient = 4), the rate constant can be amplified exponentially with [Ca²⁺]_d, which is not physiological and can result in computational instability. This differs from the kinetic properties of activation/deactivation in the model presented here which contain both fast and slow components, allowing the level of activation to respond to intra-beat Ca²⁺ dynamics (Fig. 9A) in addition to multi-beat time scales (Fig. 3C). With respect to spark generation and the role of NCX1 in the regulation of CICR and the AP, the findings presented here may not be largely dependent on the kinetic property differences between this CBD12-based model and an instantaneous formulation of allosteric NCX1 regulation [83]. However, the dynamical properties of NCX1 in this model, which differ substantially from those of Ginsburg et al. [48], are essential in order for it to play a physiological role in Ca²⁺ modulation.

The Ca²⁺-dependent allosteric regulation mechanism of this NCX1 model enables a range of activation levels that correspond to the operating ranges and waveforms of [Ca²⁺] that occur across different subcellular compartments. Allosteric regulation effectively reduces the operation of NCX1 in the cytosol, but this inhibitory mechanism is relieved in the dyad and PD where [Ca²⁺] is high. The ability of the cell to “functionally localize” NCX1 operation via this regulatory mechanism ensures cytosolic NCX1 functions at a lower capacity compared to dyadic and PD NCX1, which is important for maintaining normal cellular Ca²⁺ load and physiological Ca²⁺ transient properties.

Conclusion

Using biophysically based computational models, the multifaceted roles of NCX1 and the nature of its spatial distribution (to dyad, PD, and cytosol) in the regulation Ca²⁺ dynamics from the level of sparks to whole-cell have been demonstrated. Under physiological conditions, NCX1 primarily functions to extrude Ca²⁺ and to temper dyadic Ca²⁺ activity in diastole. On the other hand, upon sufficient membrane depolarization and/or in presence of elevated local [Na⁺], NCX1 promotes Ca²⁺ entry and contributes to triggering CICR. The whole-cell model predicts how differential placement of NCX1 into cytosolic, PD, and dyadic compartments affects the morphology of whole-cell I_{NCX1} (under AP clamp), with the best reproduction of experimental data achieved for an NCX1 distribution that matches the recent imaging data of Wang et al. [34], with a dyad-to-PD NCX1 placement ratio of ~ 1:2. Finally, allosteric Ca²⁺ activation of NCX1 helps to “functionally localize” exchanger activity to the dyad and PD by reducing exchanger activity in the cytosol thereby protecting the cell from excessive loss of Ca²⁺ during diastole.

Supplementary Material

Refer to Web version on PubMed Central for supplementary material.

Acknowledgments

The authors would like to thank W. Jonathan Lederer and G. S. Blair Williams for insightful discussions. Research supported by NIH grant R01HL105239.

Abbreviations

NCX1	Na ⁺ /Ca ²⁺ exchanger
RyR2	ryanodine receptor
CICR	Ca ²⁺ -induced Ca ²⁺ release
AP	action potential
PD	peri-dyad
<i>f_d</i>, <i>f_{pd}</i>, and <i>f_{cyto}</i>	fraction of NCX1 in dyad, PD, and cytosol

References

1. Bassani JW, Bassani RA, Bers DM. Relaxation in rabbit and rat cardiac cells: species-dependent differences in cellular mechanisms. *J Physiol*. 1994; 476:279–93. [PubMed: 8046643]
2. Mackiewicz U, Lewartowski B. Temperature dependent contribution of Ca²⁺ transporters to relaxation in cardiac myocytes: important role of sarcolemmal Ca²⁺-ATPase. *J Physiol Pharmacol*. 2006; 57:3–15. [PubMed: 16601311]
3. Kimura J, Noma A, Irisawa H. Na-Ca exchange current in mammalian heart cells. *Nature*. 1986; 319:596–7. [PubMed: 3945347]
4. Levitsky DO, Frayssé B, Leoty C, Nicoll DA, Philipson KD. Cooperative interaction between Ca²⁺-binding sites in the hydrophilic loop of the Na(+)-Ca²⁺ exchanger. *Mol Cell Biochem*. 1996; 160–161:27–32.
5. Besserer GM, Ottolia M, Nicoll DA, Chaptal V, Cascio D, Philipson KD, et al. The second Ca²⁺-binding domain of the Na⁺ Ca²⁺ exchanger is essential for regulation: crystal structures and mutational analysis. *Proc Natl Acad Sci U S A*. 2007; 104:18467–72. [PubMed: 17962412]
6. Boyman L, Mikhasenko H, Hiller R, Khananshvili D. Kinetic and equilibrium properties of regulatory calcium sensors of NCX1 protein. *J Biol Chem*. 2009; 284:6185–93. [PubMed: 19141619]
7. Giladi M, Boyman L, Mikhasenko H, Hiller R, Khananshvili D. Essential role of the CBD1-CBD2 linker in slow dissociation of Ca²⁺ from the regulatory two-domain tandem of NCX1. *J Biol Chem*. 2010; 285:28117–25. [PubMed: 20587421]
8. Hilge M, Aelen J, Perrakis A, Vuister GW. Structural basis for Ca²⁺ regulation in the Na⁺/Ca²⁺ exchanger. *Ann N Y Acad Sci*. 2007; 1099:7–15. [PubMed: 17347334]
9. Hilge M, Aelen J, Vuister GW. Ca²⁺ regulation in the Na⁺/Ca²⁺ exchanger involves two markedly different Ca²⁺ sensors. *Mol Cell*. 2006; 22:15–25. [PubMed: 16600866]
10. Ottolia M, Nicoll DA, Philipson KD. Roles of two Ca²⁺-binding domains in regulation of the cardiac Na⁺-Ca²⁺ exchanger. *J Biol Chem*. 2009; 284:32735–41. [PubMed: 19801651]
11. Chaptal V, Besserer GM, Ottolia M, Nicoll DA, Cascio D, Philipson KD, et al. How does regulatory Ca²⁺ regulate the Na⁺-Ca²⁺ exchanger? *Channels (Austin)*. 2007; 1:397–9. [PubMed: 18690047]

12. Hilge M, Aelen J, Foarce A, Perrakis A, Vuister GW. Ca²⁺ regulation in the Na⁺/Ca²⁺ exchanger features a dual electrostatic switch mechanism. *Proc Natl Acad Sci U S A*. 2009; 106:14333–8. [PubMed: 19667209]
13. Giladi M, Hiller R, Hirsch JA, Khananshvil D. Population shift underlies Ca²⁺-induced regulatory transitions in the sodium-calcium exchanger (NCX). *J Biol Chem*. 2013; 288:23141–9. [PubMed: 23798674]
14. Matsuoka S, Hilgemann DW. Steady-state and dynamic properties of cardiac sodium-calcium exchange. Ion and voltage dependencies of the transport cycle. *J Gen Physiol*. 1992; 100:963–1001. [PubMed: 1336540]
15. Matsuoka S, Nicoll DA, He Z, Philipson KD. Regulation of cardiac Na⁽⁺⁾-Ca²⁺ exchanger by the endogenous XIP region. *J Gen Physiol*. 1997; 109:273–86. [PubMed: 9041455]
16. Hilgemann DW, Collins A, Matsuoka S. Steady-state and dynamic properties of cardiac sodium-calcium exchange. Secondary modulation by cytoplasmic calcium and ATP. *J Gen Physiol*. 1992; 100:933–61. [PubMed: 1484286]
17. Fujioka Y, Hiroe K, Matsuoka S. Regulation kinetics of Na⁺-Ca²⁺ exchange current in guinea-pig ventricular myocytes. *J Physiol*. 2000; 529(Pt 3):611–23.
18. Weber CR, Ginsburg KS, Philipson KD, Shannon TR, Bers DM. Allosteric regulation of Na/Ca exchange current by cytosolic Ca in intact cardiac myocytes. *J Gen Physiol*. 2001; 117:119–31. [PubMed: 11158165]
19. Hobai IA, O'Rourke B. Enhanced Ca⁽²⁺⁾-activated Na⁽⁺⁾-Ca⁽²⁺⁾ exchange activity in canine pacing-induced heart failure. *Circ Res*. 2000; 87:690–8. [PubMed: 11029405]
20. Diaz ME, Graham HK, O'Neill SC, Trafford AW, Eisner DA. The control of sarcoplasmic reticulum Ca content in cardiac muscle. *Cell Calcium*. 2005; 38:391–6. [PubMed: 16139353]
21. Kappl M, Hartung K. Rapid charge translocation by the cardiac Na⁽⁺⁾-Ca²⁺ exchanger after a Ca²⁺ concentration jump. *Biophys J*. 1996; 71:2473–85. [PubMed: 8913587]
22. Niggli E, Lederer WJ. Molecular operations of the sodium-calcium exchanger revealed by conformation currents. *Nature*. 1991; 349:621–4. [PubMed: 2000135]
23. Miura Y, Kimura J. Sodium-calcium exchange current. Dependence on internal Ca and Na and competitive binding of external Na and Ca. *J Gen Physiol*. 1989; 93:1129–45. [PubMed: 2549177]
24. Matsuoka S, Nicoll DA, Hryshko LV, Levitsky DO, Weiss JN, Philipson KD. Regulation of the cardiac Na⁽⁺⁾-Ca²⁺ exchanger by Ca²⁺. Mutational analysis of the Ca⁽²⁺⁾-binding domain. *J Gen Physiol*. 1995; 105:403–20. [PubMed: 7769381]
25. Maack C, Ganesan A, Sidor A, O'Rourke B. Cardiac sodium-calcium exchanger is regulated by allosteric calcium and exchanger inhibitory peptide at distinct sites. *Circ Res*. 2005; 96:91–9. [PubMed: 15550690]
26. Boyman L, Hagen BM, Giladi M, Hiller R, Lederer WJ, Khananshvil D. Proton-sensing Ca²⁺-binding domains regulate the cardiac Na⁺/Ca²⁺ exchanger. *J Biol Chem*. 2011; 286:28811–20. [PubMed: 21680748]
27. Ottolia M, Philipson KD, John S. Conformational changes of the Ca⁽²⁺⁾ regulatory site of the Na⁽⁺⁾-Ca⁽²⁺⁾ exchanger detected by FRET. *Biophys J*. 2004; 87:899–906. [PubMed: 15298897]
28. Scriven DR, Dan P, Moore ED. Distribution of proteins implicated in excitation-contraction coupling in rat ventricular myocytes. *Biophys J*. 2000; 79:2682–91. [PubMed: 11053140]
29. Jayasinghe ID, Cannell MB, Soeller C. Organization of ryanodine receptors, transverse tubules, and sodium-calcium exchanger in rat myocytes. *Biophys J*. 2009; 97:2664–73. [PubMed: 19917219]
30. Dan P, Lin E, Huang J, Biln P, Tibbits GF. Three-dimensional distribution of cardiac Na⁺-Ca²⁺ exchanger and ryanodine receptor during development. *Biophys J*. 2007; 93:2504–18. [PubMed: 17557789]
31. Thomas MJ, Sjaastad I, Andersen K, Helm PJ, Wasserstrom JA, Sejersted OM, et al. Localization and function of the Na⁺/Ca²⁺-exchanger in normal and detubulated rat cardiomyocytes. *J Mol Cell Cardiol*. 2003; 35:1325–37. [PubMed: 14596789]
32. Despa S, Brette F, Orchard CH, Bers DM. Na/Ca exchange and Na/K-ATPase function are equally concentrated in transverse tubules of rat ventricular myocytes. *Biophys J*. 2003; 85:3388–96. [PubMed: 14581240]

33. Yang Z, Pascarel C, Steele DS, Komukai K, Brette F, Orchard CH. Na⁺-Ca²⁺ exchange activity is localized in the T-tubules of rat ventricular myocytes. *Circ Res*. 2002; 91:315–22. [PubMed: 12193464]
34. Wang W, Landstrom AP, Wang Q, Munro ML, Beavers D, Ackerman MJ, et al. Reduced junctional Na⁺/Ca²⁺-exchanger activity contributes to sarcoplasmic reticulum Ca²⁺ leak in junctophilin-2-deficient mice. *Am J Physiol Heart Circ Physiol*. 2014; 307:H1317–26. [PubMed: 25193470]
35. Goldhaber JI, Lamp ST, Walter DO, Garfinkel A, Fukumoto GH, Weiss JN. Local regulation of the threshold for calcium sparks in rat ventricular myocytes: role of sodium-calcium exchange. *J Physiol*. 1999; 520(Pt 2):431–8. [PubMed: 10523412]
36. Neco P, Rose B, Huynh N, Zhang R, Bridge JH, Philipson KD, et al. Sodium-calcium exchange is essential for effective triggering of calcium release in mouse heart. *Biophys J*. 2010; 99:755–64. [PubMed: 20682252]
37. Bovo E, de Tombe PP, Zima AV. The role of dyadic organization in regulation of sarcoplasmic reticulum Ca(2+) handling during rest in rabbit ventricular myocytes. *Biophys J*. 2014; 106:1902–9. [PubMed: 24806922]
38. Bouchard RA, Clark RB, Giles WR. Role of sodium-calcium exchange in activation of contraction in rat ventricle. *J Physiol*. 1993; 472:391–413. [PubMed: 8145151]
39. Sham JS, Cleemann L, Morad M. Gating of the cardiac Ca²⁺ release channel: the role of Na⁺ current and Na(+)-Ca²⁺ exchange. *Science*. 1992; 255:850–3. [PubMed: 1311127]
40. Sipido KR, Maes M, Van de Werf F. Low efficiency of Ca²⁺ entry through the Na(+)-Ca²⁺ exchanger as trigger for Ca²⁺ release from the sarcoplasmic reticulum. A comparison between L-type Ca²⁺ current and reverse-mode Na(+)-Ca²⁺ exchange. *Circ Res*. 1997; 81:1034–44. [PubMed: 9400385]
41. Litwin SE, Li J, Bridge JH. Na-Ca exchange and the trigger for sarcoplasmic reticulum Ca release: studies in adult rabbit ventricular myocytes. *Biophys J*. 1998; 75:359–71. [PubMed: 9649393]
42. Su Z, Sugishita K, Ritter M, Li F, Spitzer KW, Barry WH. The sodium pump modulates the influence of I(Na) on [Ca²⁺]_i transients in mouse ventricular myocytes. *Biophys J*. 2001; 80:1230–7. [PubMed: 11222287]
43. Wasserstrom JA, Vites AM. The role of Na(+)-Ca²⁺ exchange in activation of excitation-contraction coupling in rat ventricular myocytes. *J Physiol*. 1996; 493(Pt 2):529–42. [PubMed: 8782114]
44. Sobie EA, Cannell MB, Bridge JH. Allosteric activation of Na⁺-Ca²⁺ exchange by L-type Ca²⁺ current augments the trigger flux for SR Ca²⁺ release in ventricular myocytes. *Biophys J*. 2008; 94:L54–6. [PubMed: 18223001]
45. Viatchenko-Karpinski S, Terentyev D, Jenkins LA, Lutherer LO, Gyorke S. Synergistic interactions between Ca²⁺ entries through L-type Ca²⁺ channels and Na⁺-Ca²⁺ exchanger in normal and failing rat heart. *J Physiol*. 2005; 567:493–504. [PubMed: 15975978]
46. Walker MA, Williams GS, Kohl T, Lehnart SE, Jafri MS, Greenstein JL, et al. Superresolution modeling of calcium release in the heart. *Biophys J*. 2014; 107:3018–29. [PubMed: 25517166]
47. Greenstein JL, Winslow RL. An integrative model of the cardiac ventricular myocyte incorporating local control of Ca²⁺ release. *Biophys J*. 2002; 83:2918–45. [PubMed: 12496068]
48. Ginsburg KS, Weber CR, Bers DM. Cardiac Na⁺-Ca²⁺ exchanger: dynamics of Ca²⁺-dependent activation and deactivation in intact myocytes. *J Physiol*. 2013; 591:2067–86. [PubMed: 23401616]
49. Segel, I. *Enzyme Kinetics. Behavior and Analysis of Rapid Equilibrium and Steady-state Enzyme Systems* Johns. Wiley & Sons, Inc.; 1993. p. 957
50. Higgins ER, Goel P, Puglisi JL, Bers DM, Cannell M, Sneyd J. Modelling calcium microdomains using homogenisation. *J Theor Biol*. 2007; 247:623–44. [PubMed: 17499276]
51. Kang TM, Hilgemann DW. Multiple transport modes of the cardiac Na⁺/Ca²⁺ exchanger. *Nature*. 2004; 427:544–8. [PubMed: 14765196]
52. Keener, JP, SJ. *Mathematical Physiology*. Springer; Berlin: 1998.
53. Giladi M, Bohbot H, Buki T, Schulze DH, Hiller R, Khananshvili D. Dynamic features of allosteric Ca²⁺ sensor in tissue-specific NCX variants. *Cell Calcium*. 2012; 51:478–85. [PubMed: 22571864]

54. Weber CR, Piacentino V 3rd, Ginsburg KS, Houser SR, Bers DM. Na(+)-Ca(2+) exchange current and submembrane [Ca(2+)] during the cardiac action potential. *Circ Res.* 2002; 90:182–9. [PubMed: 11834711]
55. Lukyanenko V, Gyorke S. Ca²⁺ sparks and Ca²⁺ waves in saponin-permeabilized rat ventricular myocytes. *J Physiol.* 1999; 521(Pt 3):575–85. [PubMed: 10601490]
56. Kubalova Z, Terentyev D, Viatchenko-Karpinski S, Nishijima Y, Gyorke I, Terentyeva R, et al. Abnormal intrastore calcium signaling in chronic heart failure. *Proc Natl Acad Sci U S A.* 2005; 102:14104–9. [PubMed: 16172392]
57. Beavers DL, Wang W, Ather S, Voigt N, Garbino A, Dixit SS, et al. Mutation E169K in junctophilin-2 causes atrial fibrillation due to impaired RyR2 stabilization. *J Am Coll Cardiol.* 2013; 62:2010–9. [PubMed: 23973696]
58. Hobai IA, O'Rourke B. Decreased sarcoplasmic reticulum calcium content is responsible for defective excitation-contraction coupling in canine heart failure. *Circulation.* 2001; 103:1577–84. [PubMed: 11257088]
59. Williams GS, Chikando AC, Tuan HT, Sobie EA, Lederer WJ, Jafri MS. Dynamics of calcium sparks and calcium leak in the heart. *Biophys J.* 2011; 101:1287–96. [PubMed: 21943409]
60. Foteinou PT, Greenstein JL, Winslow RL. Mechanistic Investigation of the Arrhythmogenic Role of Oxidized CaMKII in the Heart. *Biophys J.* 2015; 109:838–49. [PubMed: 26287635]
61. Hake J, Edwards AG, Yu Z, Kekenes-Huskey PM, Michailova AP, McCammon JA, et al. Modelling cardiac calcium sparks in a three-dimensional reconstruction of a calcium release unit. *J Physiol.* 2012; 590:4403–22. [PubMed: 22495592]
62. Hilgemann DW. Unitary cardiac Na⁺, Ca²⁺ exchange current magnitudes determined from channel-like noise and charge movements of ion transport. *Biophys J.* 1996; 71:759–68. [PubMed: 8842214]
63. O'Rourke B, Kass DA, Tomaselli GF, Kaab S, Tunin R, Marban E. Mechanisms of altered excitation-contraction coupling in canine tachycardia-induced heart failure, I: experimental studies. *Circ Res.* 1999; 84:562–70. [PubMed: 10082478]
64. Bers DM., SpringerLink (Online service). *Developments in Cardiovascular Medicine.* Second. Dordrecht: Springer; Netherlands: Imprint: Springer; 2001. Excitation-Contraction Coupling and Cardiac Contractile Force; p. 1online resource
65. Acsai K, Antoons G, Livshitz L, Rudy Y, Sipido KR. Microdomain [Ca(2+)] near ryanodine receptors as reported by L-type Ca(2+) and Na+/Ca(2+) exchange currents. *J Physiol.* 2011; 589:2569–83. [PubMed: 21486798]
66. Livshitz L, Acsai K, Antoons G, Sipido K, Rudy Y. Data-based theoretical identification of subcellular calcium compartments and estimation of calcium dynamics in cardiac myocytes. *J Physiol.* 2012; 590:4423–46. [PubMed: 22547631]
67. Hilgemann DW, Collins A, Cash DP, Nagel GA. Cardiac Na(+)-Ca²⁺ exchange system in giant membrane patches. *Ann N Y Acad Sci.* 1991; 639:126–39. [PubMed: 1785836]
68. Fang Y, Condrescu M, Reeves JP. Regulation of Na⁺/Ca²⁺ exchange activity by cytosolic Ca²⁺ in transfected Chinese hamster ovary cells. *Am J Physiol.* 1998; 275:C50–5. [PubMed: 9688834]
69. Collins A, Somlyo AV, Hilgemann DW. The giant cardiac membrane patch method: stimulation of outward Na(+)-Ca²⁺ exchange current by MgATP. *J Physiol.* 1992; 454:27–57. [PubMed: 1335502]
70. Trac M, Dyck C, Hnatowich M, Omelchenko A, Hryshko LV. Transport and regulation of the cardiac Na(+)-Ca²⁺ exchanger, NCX1. Comparison between Ca²⁺ and Ba²⁺ *J Gen Physiol.* 1997; 109:361–9. [PubMed: 9089442]
71. John SA, Ribalet B, Weiss JN, Philipson KD, Ottolia M. Ca²⁺-dependent structural rearrangements within Na⁺-Ca²⁺ exchanger dimers. *Proc Natl Acad Sci U S A.* 2011; 108:1699–704. [PubMed: 21209335]
72. Grantham CJ, Cannell MB. Ca²⁺ influx during the cardiac action potential in guinea pig ventricular myocytes. *Circ Res.* 1996; 79:194–200. [PubMed: 8755995]
73. duBell WH, Boyett MR, Spurgeon HA, Talo A, Stern MD, Lakatta EG. The cytosolic calcium transient modulates the action potential of rat ventricular myocytes. *J Physiol.* 1991; 436:347–69. [PubMed: 2061836]

74. Luo CH, Rudy Y. A dynamic model of the cardiac ventricular action potential. I. Simulations of ionic currents and concentration changes. *Circ Res.* 1994; 74:1071–96. [PubMed: 7514509]
75. Sher AA, Noble PJ, Hinch R, Gavaghan DJ, Noble D. The role of the Na⁺/Ca²⁺ exchangers in Ca²⁺ dynamics in ventricular myocytes. *Prog Biophys Mol Biol.* 2008; 96:377–98. [PubMed: 17959231]
76. Larbig R, Torres N, Bridge JH, Goldhaber JI, Philipson KD. Activation of reverse Na⁺-Ca²⁺ exchange by the Na⁺ current augments the cardiac Ca²⁺ transient: evidence from NCX knockout mice. *J Physiol.* 2010; 588:3267–76. [PubMed: 20643777]
77. Torres NS, Larbig R, Rock A, Goldhaber JI, Bridge JH. Na⁺ currents are required for efficient excitation-contraction coupling in rabbit ventricular myocytes: a possible contribution of neuronal Na⁺ channels. *J Physiol.* 2010; 588:4249–60. [PubMed: 20837647]
78. Leblanc N, Hume JR. Sodium current-induced release of calcium from cardiac sarcoplasmic reticulum. *Science.* 1990; 248:372–6. [PubMed: 2158146]
79. Blaustein MP, Lederer WJ. Sodium/calcium exchange: its physiological implications. *Physiol Rev.* 1999; 79:763–854. [PubMed: 10390518]
80. Verdonck F, Mubagwa K, Sipido KR. [Na(+)] in the subsarcolemmal ‘fuzzy’ space and modulation of [Ca(2+)](i) and contraction in cardiac myocytes. *Cell Calcium.* 2004; 35:603–12. [PubMed: 15110150]
81. Lederer WJ, Niggli E, Hadley RW. Sodium-calcium exchange in excitable cells: fuzzy space. *Science.* 1990; 248:283. [PubMed: 2326638]
82. Wendt-Gallitelli MF, Voigt T, Isenberg G. Microheterogeneity of subsarcolemmal sodium gradients. Electron probe microanalysis in guinea-pig ventricular myocytes. *J Physiol.* 1993; 472:33–44. [PubMed: 8145148]
83. Weber CR, Piacentino V 3rd, Houser SR, Bers DM. Dynamic regulation of sodium/calcium exchange function in human heart failure. *Circulation.* 2003; 108:2224–9. [PubMed: 14557358]

Highlights

- A novel mechanistic and biophysically-detailed model is formulated describing both the transport kinetics and dynamic Ca^{2+} -dependent allosteric regulation of NCX1.
- This NCX1 model is incorporated into both a super-resolution model of Ca^{2+} spark generation and a stochastic whole-cell model of canine ventricular myocytes in order to study the effects of preferential placement of NCX1 within and near the cardiac dyad.
- Both models predict that Ca^{2+} spark frequency, fidelity, and diastolic Ca^{2+} levels are strong decreasing functions of the fraction of NCX1 localized to the dyad and PD, and that spark amplitude and duration are less sensitive to this fraction.
- Whole-cell modeling of NCX1 tail currents are consistent with recent super-resolution imaging studies showing a high fraction of NCX1 (~45%) reside in the t-tubules with a dyad-to-PD ratio of roughly 1:2.

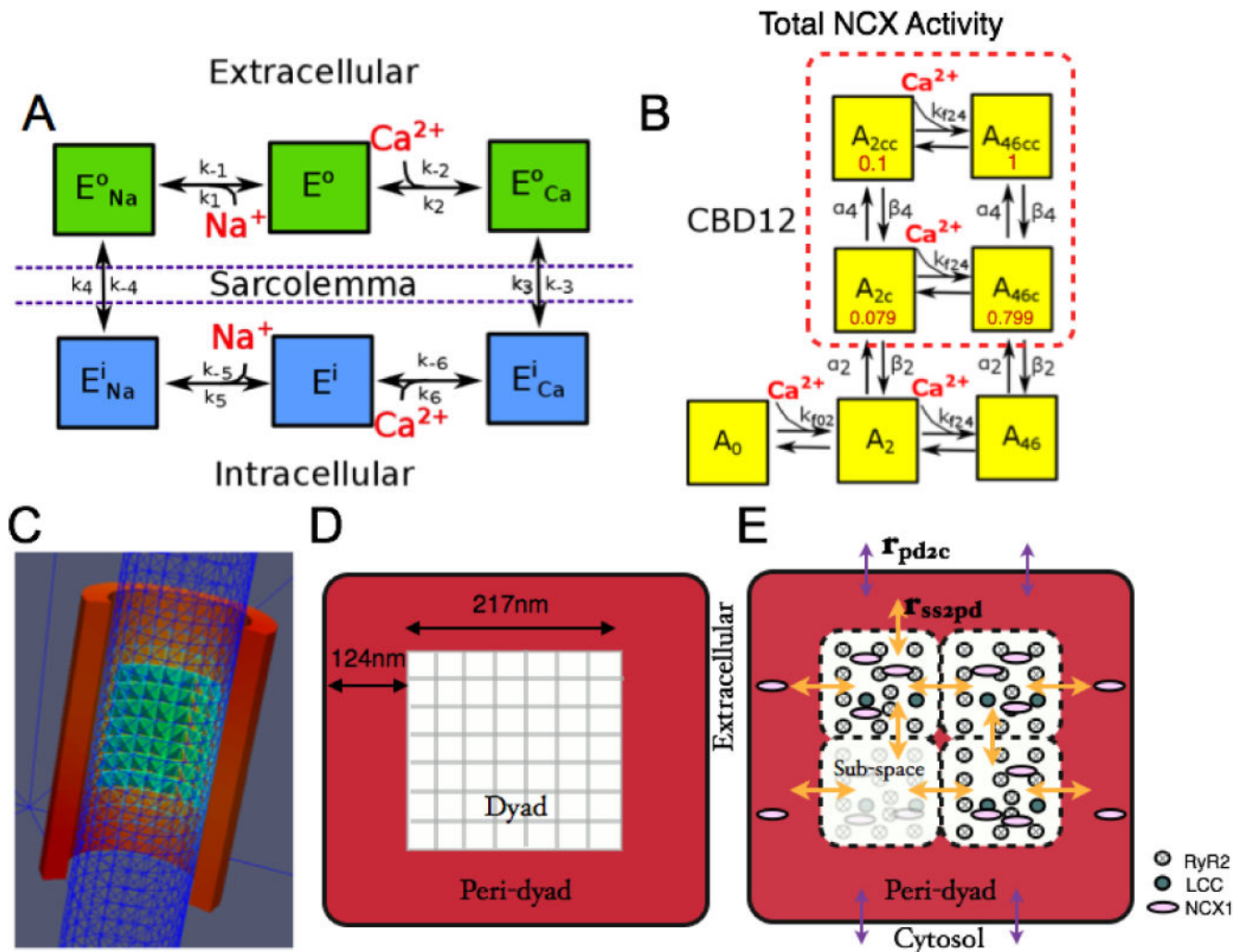


Figure 1. NCX1 kinetic schemes and dyad model geometry. (A) State model for NCX1 transport kinetics. (B) State model for CBD12 Ca^{2+} -dependent allosteric regulation with partial activity coefficients (red). (C) 3D mesh from SRS model [46] showing a t-tubule modeled as a cylinder (blue) partially encircled by JSR (red) containing a cluster of RyR2s (green-blue), forming a dyadic space with a 15 nm gap between these membranes. (D) Illustration of flattened JSR from the SRS model with a centered 7x7 RyR2 lattice. (E) A t-tubule-JSR cleft (or CRU) of the whole-cell model (shown in cross-section) is composed of four dyadic subspace volumes arranged on a 2x2 grid, each containing 2 LCCs and 12 RyR2s. The PD is a single compartment that surrounds the subspace grid (i.e. the dyad).

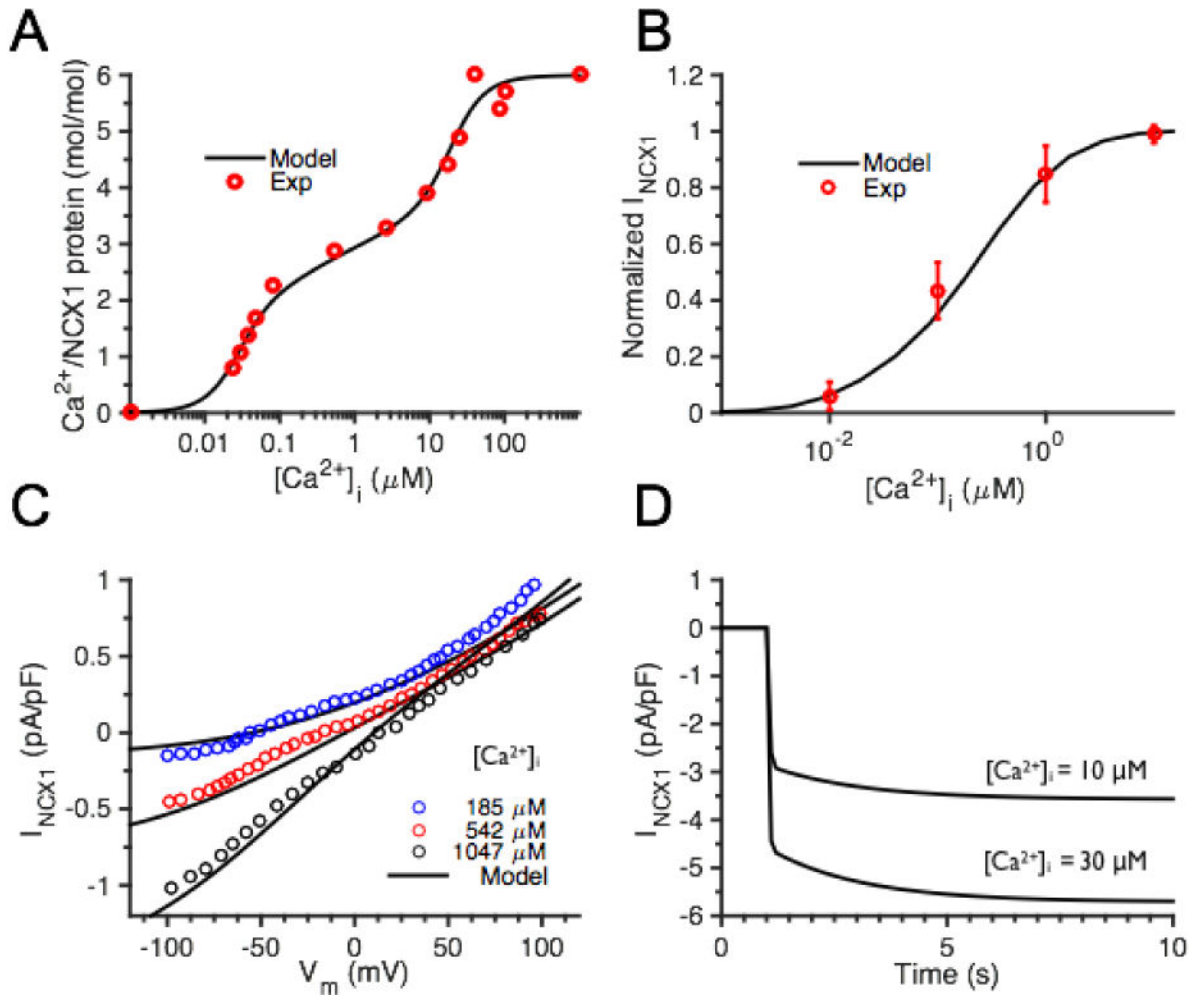


Figure 2. NCX1 model constraint and validation. (A) CBD12 model constraint: Ca²⁺ binding site steady state occupancy compares to experimental data of Giladi et al. [7]. (B) Model NCX1 fractional activity compared with experimental data [17]. (C) Steady state NCX1 I–V curve validation against whole-cell patch clamp results under various [Ca²⁺]_i [54]. (D). Fast and slow phases of NCX1 model activation time-course in response to [Ca²⁺]_i clamp to indicated value at (at 1 s) resembles those of Fujioka et al. [17] (not shown).

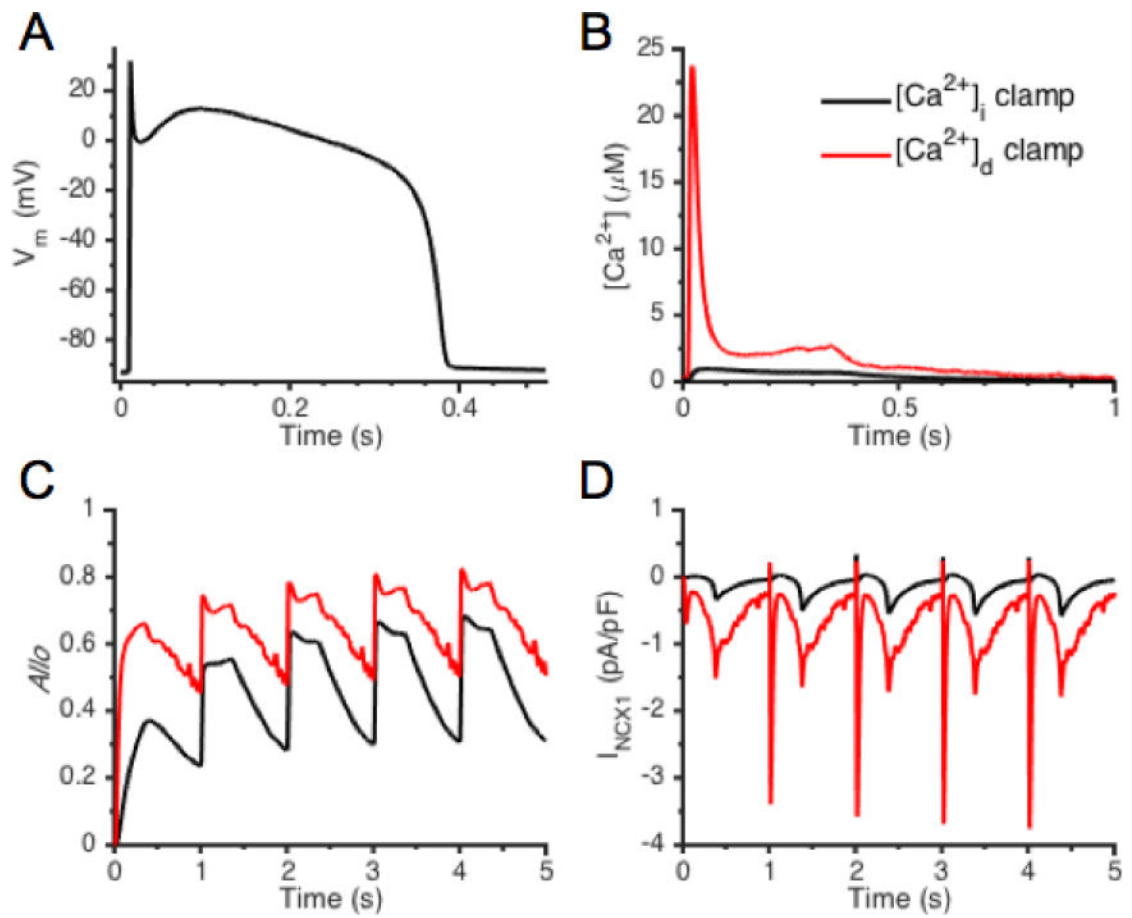


Figure 3. NCX1 dynamics driven by AP and $[Ca^{2+}]$ clamp. (A) Baseline AP-clamp V_m generated by a previous whole-cell model [60], and (B) corresponding $[Ca^{2+}]_i$ and $[Ca^{2+}]_d$ signals. NCX1 allosteric factor, $Allo$ (C), and I_{NCX1} (D) underlying APs paced from rest.

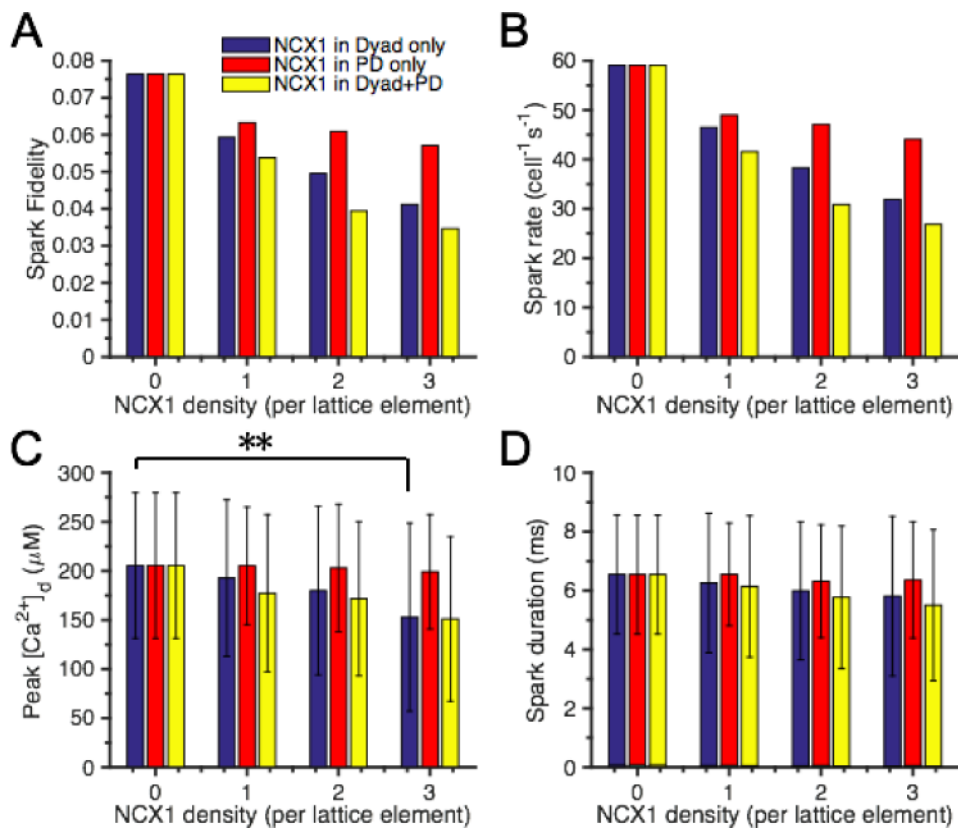


Figure 4. Effects of NCX1 on SRS model Ca²⁺ sparks. Spark fidelity simulations were initiated by opening a single random RyR2. NCX1s were placed in the dyad only (blue bars), PD only (red bars), or both (yellow bars). (A) Predicted spark fidelity. (B) Spark rate. (C) Spark amplitude measured as peak [Ca²⁺]_d, ** indicates statistically significant difference based on t-test (p < 0.05). (D) Spark duration measured as FDHM.

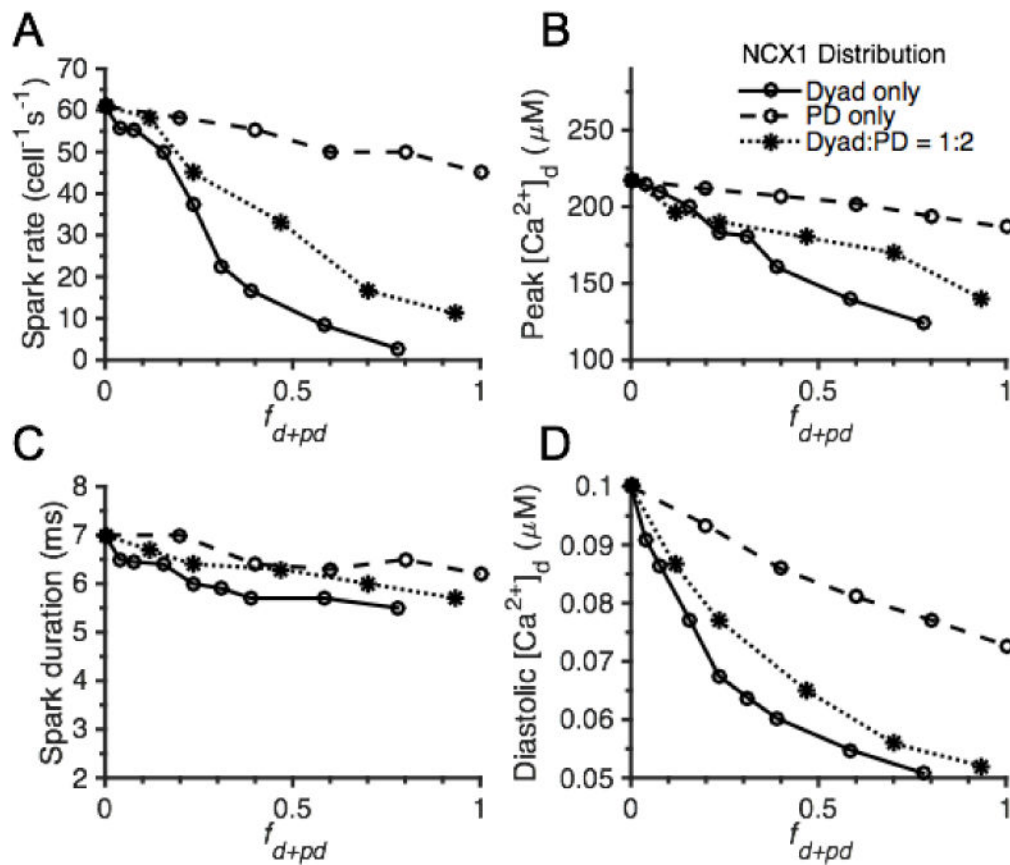


Figure 5. Effects of NCX1 localization on spark properties in the whole-cell model. The role of NCX1 distribution between cytosol and dyad only ($f_{d+pd} = f_d$ since $f_{pd} = 0$, solid lines), between cytosol and PD only ($f_{d+pd} = f_{pd}$ since $f_d = 0$, dashed lines), or among all three compartments with a $f_d:f_{pd}$ ratio of 1:2 ($f_{d+pd} = f_d + f_{pd}$ with $f_{pd} = 2f_d$, dotted lines) on whole-cell spark rate (A), peak $[\text{Ca}^{2+}]_d$ (B), spark duration measured as FDHM (C), and diastolic $[\text{Ca}^{2+}]_d$ (D). The total number of NCX1s in the cell is the same in all cases.

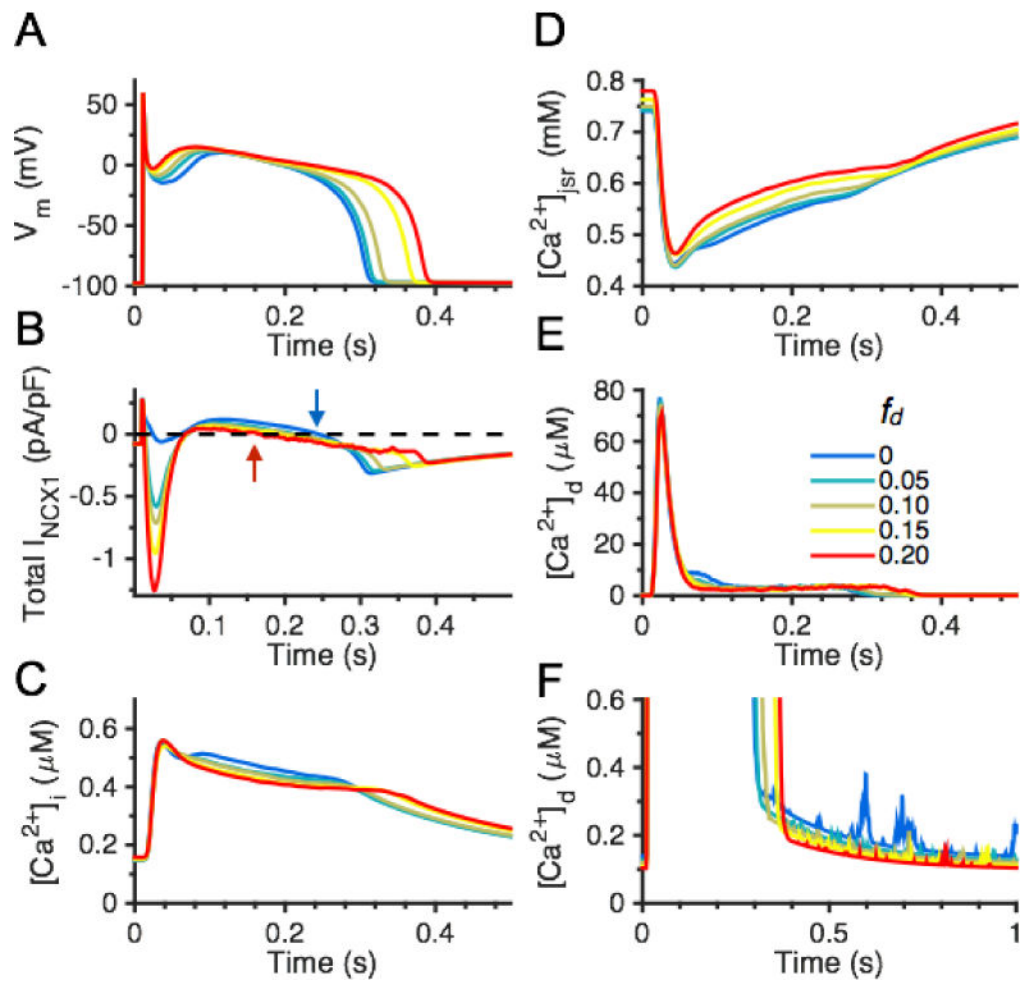


Figure 6. Effects of various dyadic NCX1 distributions (f_d values of 0, 0.05, 0.10, 0.15, and 0.20) on APs and Ca^{2+} handling with no PD NCX1. (A) APs; and (B) whole-cell I_{NCX1} . Arrows indicate time of E_{NCX1} crossing for $f_d = 0$ (blue) and $f_d = 0.2$ (red). (C) Cytosolic Ca^{2+} transient $[Ca^{2+}]_i$. (D) $[Ca]_{jSr}$. (E) $[Ca^{2+}]_d$. (F) Diastolic phase of $[Ca^{2+}]_d$.

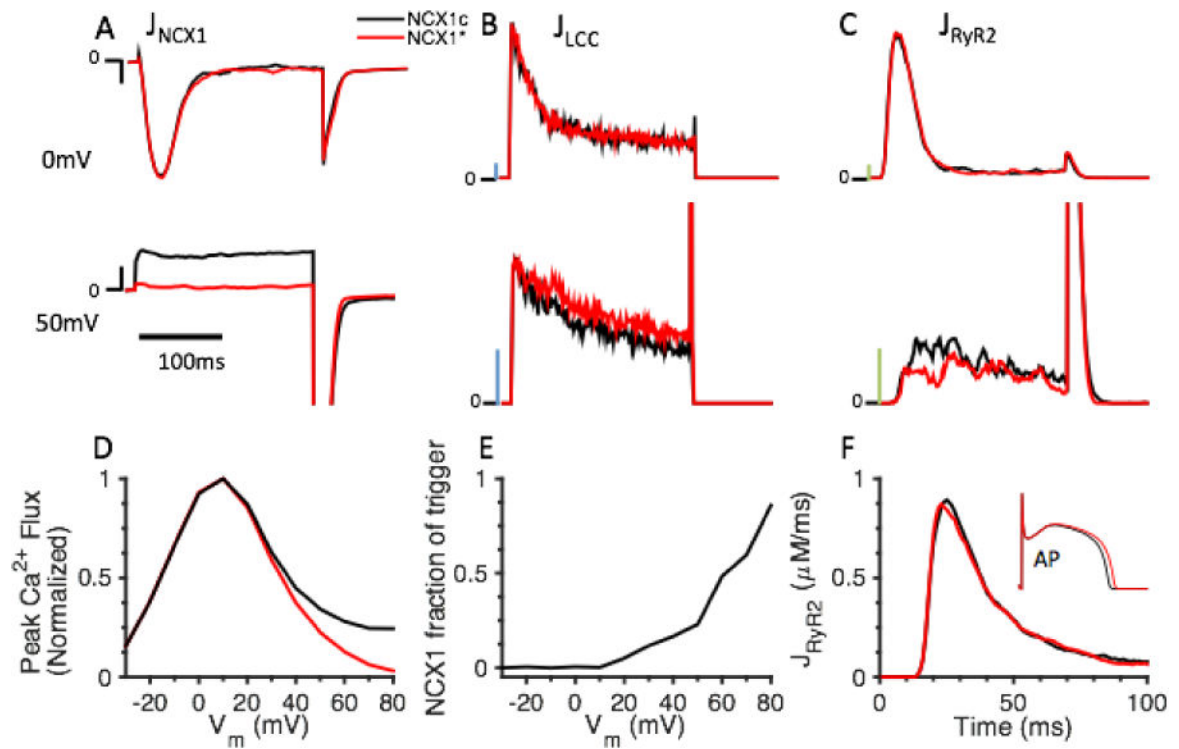


Figure 7.

The CICR triggering capacity of NCX1. (A–D) Test potentials to 0 mV and 50 mV of 200 ms duration were applied to the whole-cell model from a holding potential of –90 mV under NCX1c (control NCX1, black lines) or NCX1* (reverse mode NCX1 clamped to zero, red lines) conditions. (A) J_{NCX1} , scale bar (black): 0.01 $\mu M/ms$. (B) J_{LCC} , scale bar (blue): 0.1 $\mu M/ms$. (C) J_{RyR2} , scale bar (green): 1 $\mu M/ms$. (D) Normalized peak Ca^{2+} influx ($J_{LCC} + J_{NCX1}$) in response to test potentials from –30 mV to 80 mV for NCX1c (black) and NCX1* (red). The results suggest that NCX1 can trigger CICR consistent with experiments [44]. (E) NCX1 fraction of CICR trigger. (F) J_{RyR2} during AP.

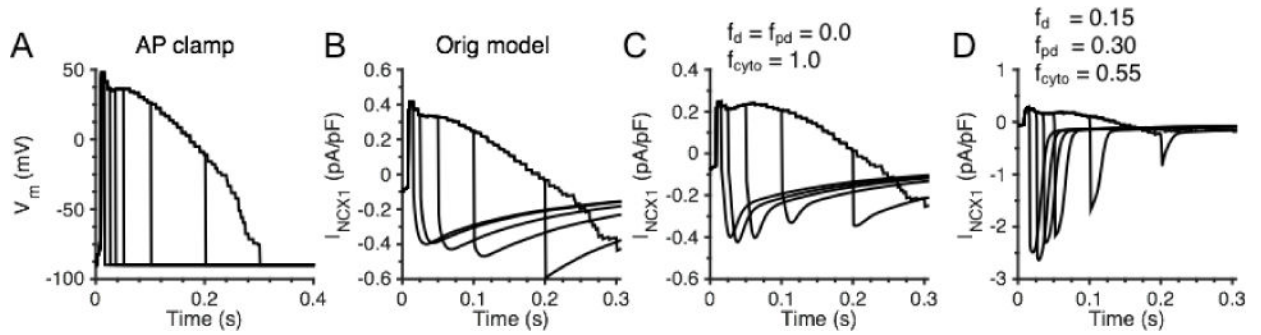


Figure 8. NCX1 tail currents under AP-clamp. (A) AP clamp recording in a rabbit ventricular myocytes from Weber et al. [54]. (B) Model prediction of NCX1 tail currents upon AP-clamp interruption at various times (10, 25, 50, 100, 200, and 300 ms) with original Greenstein and Winslow [47] model. (C) Model prediction of NCX1 tail currents with $f_{cyto} = 1.0$ (100% NCX1 in cytosol). (D) Model prediction of whole-cell NCX1 tail currents with f_d , f_{pd} , and f_{cyto} values of 0.15, 0.30, and 0.55, respectively (dyad-to-PD ratio of 1:2).

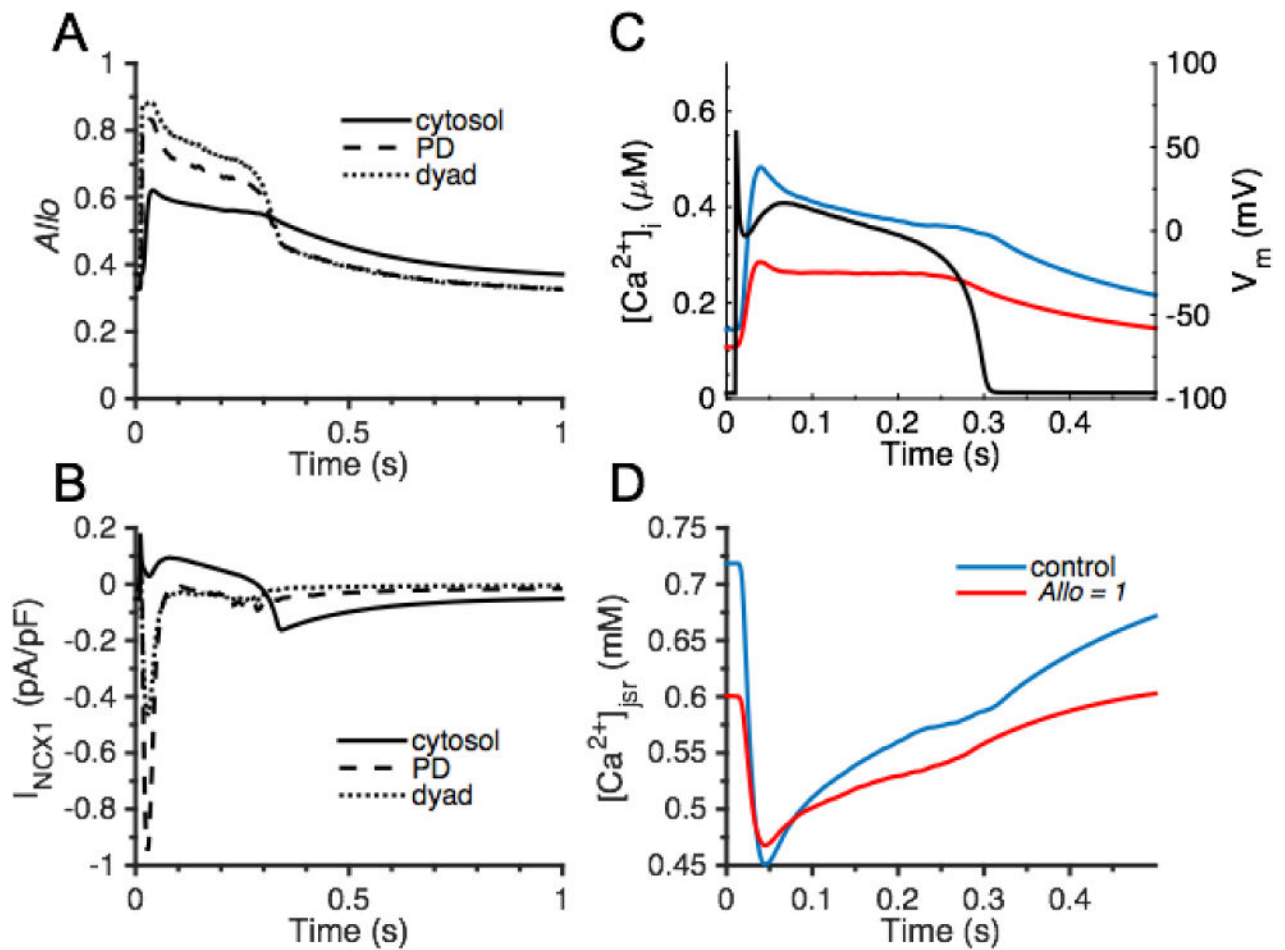


Figure 9. The beat-to-beat role of NCX1 Ca^{2+} -dependent allosteric regulation. (A) CBD12 allosteric regulation of NCX1 in cytosol (solid line), PD (dashed line), and dyad (dotted line). (B) I_{NCX1} in cytosol, PD, and dyad. (C) $[Ca^{2+}]_i$ and V_m (black) and (D) $[Ca^{2+}]_{j_{sr}}$ comparisons between control (blue) and fully active NCX1 ($Allo = 1$, red).